

# Ion acceleration by an ultrashort laser pulse interacting with a near-critical-density gas jet

M. Ehret,<sup>1,2, a)</sup> C. Salgado-López,<sup>3,4, b)</sup> V. Ospina-Bohórquez,<sup>1,4,5, c)</sup> J. A. Perez-Hernández,<sup>3</sup> M. Huault,<sup>3,4</sup> M. de Marco,<sup>3</sup> J. I. Apiñaniz,<sup>3</sup> F. Hannachi,<sup>6</sup> D. De Luis,<sup>3</sup> J. Hernández Toro,<sup>3</sup> D. Arana,<sup>3</sup> C. Méndez,<sup>3</sup> O. Varela,<sup>3</sup> A. Debayle,<sup>5,7</sup> L. Gremillet,<sup>5,7</sup> T.-H. Nguyen-Bui,<sup>1</sup> E. Olivier,<sup>1</sup> G. Revet,<sup>1</sup> N. D. Bukharskii,<sup>8</sup> H. Larreur,<sup>1</sup> J. Caron,<sup>9</sup> C. Vlachos,<sup>1,10</sup> T. Ceccotti,<sup>11</sup> D. Raffestin,<sup>1</sup> P. Nicolai,<sup>1</sup> J.L. Feugeas,<sup>1</sup> M. Roth,<sup>2</sup> X. Vaisseau,<sup>5</sup> G. Gatti,<sup>3</sup> L. Volpe,<sup>3,12</sup> and J. J. Santos<sup>1, d)</sup>

<sup>1)</sup> *Université de Bordeaux, CNRS, CEA, CELIA (Centre Lasers Intenses et Applications), UMR 5107, Talence, France*

<sup>2)</sup> *Institut für Kernphysik, Technische Universität Darmstadt, Darmstadt, Germany*

<sup>3)</sup> *C.L.P.U. (Centro de Láseres Pulsados), Salamanca, Spain*

<sup>4)</sup> *Universidad de Salamanca, Salamanca, Spain*

<sup>5)</sup> *CEA, DAM, DIF, F-91297 Arpajon, France*

<sup>6)</sup> *CENBG, CNRS-IN2P3, Université de Bordeaux, Gradignan, France*

<sup>7)</sup> *Université Paris-Saclay, CEA, LMCE, 91680 Bruyères-le-Châtel, France*

<sup>8)</sup> *National Research Nuclear University MEPhI, Moscow, Russian Federation*

<sup>9)</sup> *Institut Bergonié, Département de Radiothérapie, Unité de Radiophysique, Bordeaux, France*

<sup>10)</sup> *Centre for Plasma Physics and Lasers (CPPL), T.E.I. of Crete, Rethymnon, Greece*

<sup>11)</sup> *CEA/IRAMIS, SPAM, Gif-sur-Yvette, France*

<sup>12)</sup> *Laser-Plasma Chair at Universidad de Salamanca, Salamanca, Spain*

We demonstrate laser-driven Helium ion acceleration with cut-off energies above 25 MeV and peaked ion number above  $10^8 \text{ MeV}^{-1}$  for 22(2) MeV projectiles from near-critical density gas jet targets. We employed shock gas jet nozzles at the high-repetition-rate (HRR) VEGA-2 laser system with 3 J in pulses of 30 fs focused down to intensities in the range between  $9 \times 10^{19} \text{ Wcm}^{-2}$  and  $1.2 \times 10^{20} \text{ Wcm}^{-2}$ . We demonstrate acceleration spectra with minor shot-to-shot changes for small variations in the target gas density profile. Difference in gas profiles arise due to nozzles being exposed to a experimental environment, partially ablating and melting.

## I. INTRODUCTION

Since the advent of high-power, short-pulse lasers<sup>1</sup>, much effort has been devoted to the development of high-energy, high-quality laser-driven ion sources<sup>2,3</sup>. The interest in these sources stems from their many potential applications, including time-resolved probing of laser-induced phenomena<sup>4-6</sup>, isochoric heating of dense plasmas<sup>7</sup>, fast ignition of inertial confinement fusion targets<sup>8</sup>, nuclear physics<sup>9</sup> or medical purposes<sup>10,11</sup>. Most of these applications exploit the unique properties of laser-driven ion beams, notably their short duration, high number density, high laminarity and compactness.

The laser interactions giving rise to ion acceleration can occur in two main regimes, depending on the transparency/opacity properties of the irradiated (and ionized) medium. Solid or liquid targets with electron densities ( $n_e$ ) larger than the critical density ( $n_c = 1.7 \times 10^{21} \text{ cm}^{-3}$  for the central  $0.8 \mu\text{m}$  wavelength of a Ti:Sa laser) are opaque to the laser light, yet a significant ( $\sim 1 - 50\%$ ) fraction of the laser energy can convert into high-energy ( $\sim \text{MeV}$ ) electrons at the target

surface. When propagating across the target, these fast electrons can induce strong charge-separation fields at the target/vacuum interfaces capable of accelerating the surface ions (mainly protons) to high (up to  $\sim 100 \text{ MeV}$ ) energies<sup>12,13</sup>. This process, referred to as target normal sheath acceleration (TNSA), is the most widely studied and exploited method for laser-based ion acceleration<sup>2,3</sup>.

In dilute gaseous targets ( $n_e \ll n_c$ ), the laser pulse can propagate large distances through the plasma while generating a nonlinear wakefield that is able to accelerate some bulk electrons to ultrarelativistic energies<sup>14</sup>. Simultaneously, the transverse ponderomotive force of the focused laser pulse tends to expel radially the bulk electrons, thus creating a positively charged plasma channel. The related electrostatic fields can accelerate the plasma ions to MeV-range energies in the transverse plane<sup>15-17</sup>.

Fewer studies have addressed the case of short laser pulses interacting with plasmas of electron density  $n_e \sim 0.1 - 1 n_c$ , mostly due to the experimental difficulty of achieving such conditions in a controlled manner. This so-called near-critical interaction regime, however, is spurring increasing interest because it is predicted to optimize the energy coupling between the laser and the plasma<sup>18-22</sup>. An intense laser pulse impinging onto a near-critical plasma can drive a strong charge separation in the longitudinal direction, launching an electrostatic shock wave<sup>23-26</sup>. The supersonic propagation of this structure through the plasma goes along with par-

<sup>a)</sup> Electronic mail: michael.ehret@u-bordeaux.fr

<sup>b)</sup> Electronic mail: csalgado@clpu.es

<sup>c)</sup> Electronic mail: valeria.ospina-bohorquez@u-bordeaux.fr

<sup>d)</sup> Electronic mail: joao.santos@u-bordeaux.fr

tial reflection of the background ions at twice the shock velocity, a mechanism termed collisionless shock acceleration (CSA). The charge separation underpinning the shock formation can be driven either directly by the laser, via its ponderomotive push on the opaque region (if any) of the plasma profile<sup>19,27–31</sup>, or indirectly, via the pressure gradients associated with the laser heating of the bulk electrons in a fully transparent, nonuniform plasma<sup>20,32–34</sup>. Depending on the gas profile, CSA may come along with additional acceleration mechanisms, such as TNSA<sup>19,28</sup> or magnetic vortex acceleration<sup>35–39</sup>.

The laboratory production of near-critical plasmas remains a nontrivial task, especially when high-repetition-rate ion sources are needed. The use of widely available near-infrared ultrashort pulses requires electron plasma densities of the order of  $10^{20-21} \text{ cm}^{-3}$ , which nowadays can be achieved by means of exploding foils (using either the pedestal of the laser pulse or an additional pulse)<sup>31,32,40,41</sup>, foam targets<sup>18,21,42</sup>, nanowire arrays<sup>43,44</sup>, or high-density gas jets<sup>33,45,46</sup>. In this paper, we report on experimental measurements of the interaction of an ultrashort (30 fs), ultraintense ( $\sim 10^{20} \text{ Wcm}^{-2}$ ) laser pulse with a high-density gas jet which, once fully ionized, can attain a maximum electron density close to the critical density<sup>47</sup>.

This paper is organized as follows. The experimental setup is explained in Section II. The main experimental results, divided in two different studies, are presented in detail in Section III. The particle-in-cell (PIC) simulation results are summarized in Section IV. Finally, the conclusions and foreseen applications are outlined in Sections V and VI, respectively. Additional material regarding laser diagnostics and data analysis can be found in Section VIII.

## II. EXPERIMENTAL SETUP

The experiment was performed using the VEGA 2 Ti:Sa laser system at the Centro de Láseres Pulsados (CLPU)<sup>48</sup> in September 2018. The laser pulse, of  $3 \pm 0.36 \text{ J}$  energy, 30 fs duration and  $0.8 \mu\text{m}$  wavelength, was focused by a  $F/4$  off-axis parabolic (OAP) gold-coated mirror into the gas, see Fig. 1(a). The focal spot was consistently measured at low energy by a high magnification imaging system. A reproducible full width at half maximum (FWHM) of  $7 \mu\text{m}$  was obtained, yielding a maximum intensity between  $9 \times 10^{19} \text{ Wcm}^{-2}$  and  $1.2 \times 10^{20} \text{ Wcm}^{-2}$  at full pulse energy. The amplified stimulated emission (ASE) was characterized by an intensity contrast of  $\sim 5 \times 10^{-12}$  at  $t = -100 \text{ ps}$  (before the pulse maximum), as measured through third-order autocorrelation, see Fig. 2. The contrast was found to be  $\sim 8 \times 10^{-9}$  at  $t = -10 \text{ ps}$  and  $\sim 5 \times 10^{-8}$  at  $t = -5 \text{ ps}$ , prior to the high intensity peak.

We employed a high-pressure gas jet target developed by SourceLab<sup>47</sup>, comprising a shock-geometry nozzle attached to a rapid electro-valve with 400 bar of gas back-

ing pressure. This yielded a narrow density profile of approximately  $100 \mu\text{m}$  FWHM across the shocked region at a height of  $\approx 470 \mu\text{m}$  in respect to the nozzle extremity surface [see Figs. 1(d) and (e)]. At full ionization, the peak electron density reached  $n_e = 2.8 \times 10^{21} \text{ cm}^{-3}$ , that is, slightly above the critical density associated with a  $0.8 \mu\text{m}$  laser. Before each shot, the gas jet was characterized through interferometry using the commercially available SID-4 wavefront sensor (PHASICS)<sup>49</sup>. The nozzle was also visually inspected so as to ensure that neither its surface nor its cylindrical geometry had been altered. Several types of gas were studied: Helium (He), Nitrogen (N), and a 9/1 Nitrogen/Helium molecular density ratio gas mixture. The addition of N, due to its fluid properties, proved to be beneficial for the proper operation of the valve. A three-axis motorization system for the valve holder and two perpendicular imaging systems allowed the density peak to coincide with the laser spot in vacuum.

Main diagnostics are on-shot interferometry to determine the driven plasma density, the streaked imaging of plasma self-emission to identify hot plasma regions, and passive particle detectors as well as HRR ready time-of-flight (ToF) detectors to measure ion beam spectra.

Frequency-doubled ultra-short pick-up probe is derived from the edge of the main laser pulse. Synchronization with the main beam is done with the help of a delay line and a streak camera. We observe the plasma dynamics perpendicularly to the main driver beam axis, around 1 ns after its arrival. One half of the probe beam is aligned to propagate through free space, the other portion encounters a different optical path going through the density profile. The resulting phase shift was measured with a Nomarsky interferometer, see figure 1 b). Knowing the relation between index of refraction of a plasma and its density, and imposing cylindrical symmetry around the laser axis, one deconvolutes the ultrafast time-resolved density map of the plasma<sup>50</sup> [see Fig. 1(b)].

A fast streak camera (Hamamatsu C7700), with ps resolution, measured the plasma self-emission under an angle of  $82^\circ$  with respect to the main laser axis in the horizontal plane, blocking the NIR photons with a BG38 filter. This restriction to optical photons is a measure to protect the streak camera from scattered light of the driver laser. A line-out of the prompt self emission in arbitrary units is superposed to the interferometry in figure 1 b). Noteworthy, self emission is prominent at both ends of the plasma channel, but not at the position where the laser focus was encountered without gas.

On-line energy spectra of the accelerated particles were acquired by two Silicon PIN photodiode ToF detectors. Both photodiodes were located vertically inclined with  $19^\circ$  at 67 cm from the interaction point at different horizontal angles of (A)  $16^\circ$  and (B)  $106^\circ$  with respect to the driver laser propagation axis (see figure 1.a). The diode substrate is preceded by a Silicon layer of 750 nm and extra filtering by Mylar foils with 40 nm thick Aluminium coating, in order to avoid diode saturation by the strong

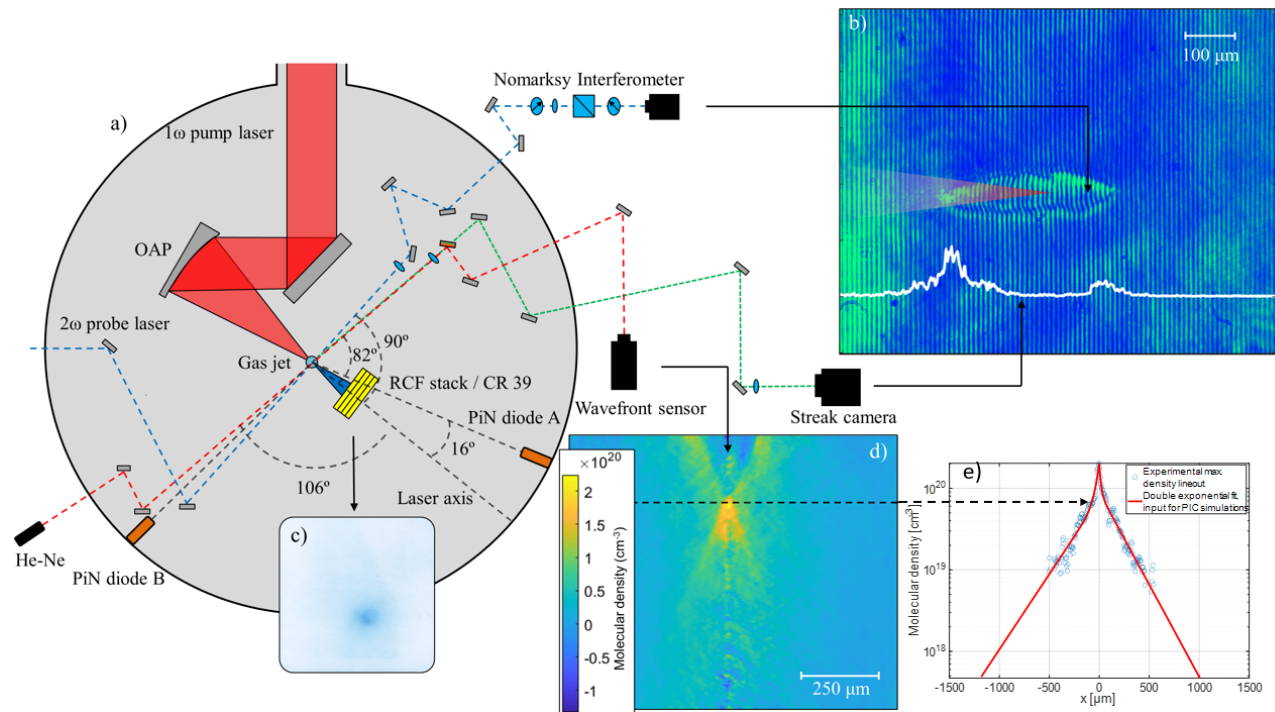


Figure 1. (a) Experimental setup top view. (b) Raw data of the interferometer. Overlaid are a lineout of the plasma self-emission as measured (arb. units) by the streak camera (white curve) and a sketch of the laser envelope in vacuum (transparent red triangle). The laser focal spot in vacuum coincides with the shocked gas region. (c) Typical RCF signal. (d) Molecular density map of the 9/1 Nitrogen/Helium molecular density ratio gas jet prior to interaction, as measured by the wavefront sensor (nozzle output is located  $300\ \mu\text{m}$  above the image). (e) Molecular density lineout at the shock height (circles) and double exponential fit of the measured data (solid line) extrapolated until  $n_{mol,min} = 5 \times 10^{17}\ \text{cm}^{-3}$  for numerical purposes (see Section IV).

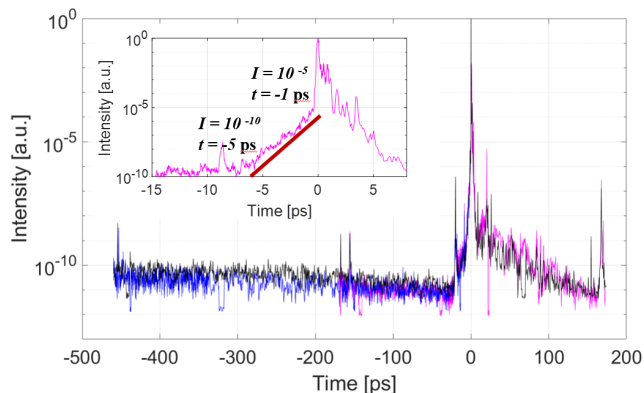


Figure 2. Three independent third-order autocorrelator (Sequoia) measurements of the temporal contrast at best compression with a  $10^{-10}$  to  $10^{-11}$  ASE level. Inset zooms in the  $\approx 5$  ps long intensity ramp prior to the arrival of the main intensity peak. For more details see Section VIII A

photopeak from the laser-target interaction. Mylar foils were (A)  $2\ \mu\text{m}$  and (B)  $4\ \mu\text{m}$  thick. Signal acquisition with a 1 GHz oscilloscope (Tektronix DPO4104) was performed at a maximum sampling rate of 200 ps per sample. 20 dB attenuation was applied to both channels. For de-

tails on data analysis, see additional material in section VIII–VIII B.

We employed solid state passive particle detectors to capture the spatial and spectral properties of forward accelerated ion beams in single-shots, with stacks of Radiochromic Films (RCF)<sup>51</sup> and slaps of Columbia Resin #39 (CR-39)<sup>52,53</sup>. RCF undergo a color-changing radiosynthesis that allows to retrieve the dose-depth curve and therewith an absolute projectile number spectrum, given the projectile species is known. To identify the projectile species, we make use of CR-39 as solid state track detector. CR-39 is especially used to distinguish ions from electrons, as projectiles with a low linear energy transfer (LET) of  $10\ \text{keV}\ \mu\text{m}^{-1}$  to  $15\ \text{keV}\ \mu\text{m}^{-1}$  from projectile to detector, typical for single electrons, do not lead to the formation of tracks<sup>54</sup>.

As RCF we used two different types of GAFCHROMIC film (Ashland), commercially available EBT-3<sup>55</sup> and specially manufactured U-EBT-3<sup>56</sup>. For details on RCF data analysis, see section VIII–VIII C 1. Each RCF stack comprises 4 layers of U-EBT-3 and 2 layers of EBT-3 and is enveloped in  $10\ \mu\text{m}$  Aluminium filter foil. Active layers of U-EBT-3 face the interaction point. CR-39 were of type TasTrak CR-39 Plastic Sheet bought in February 2015. CR-39 are enveloped in an opaque Aluminium coated

2  $\mu\text{m}$  thick Mylar foil. For more details on CR-39 data analysis, see VIII–VIII C 2.

The passive particle detector surfaces are aligned 60 mm from the interaction point - and detector slaps are perpendicular to the laser axis.

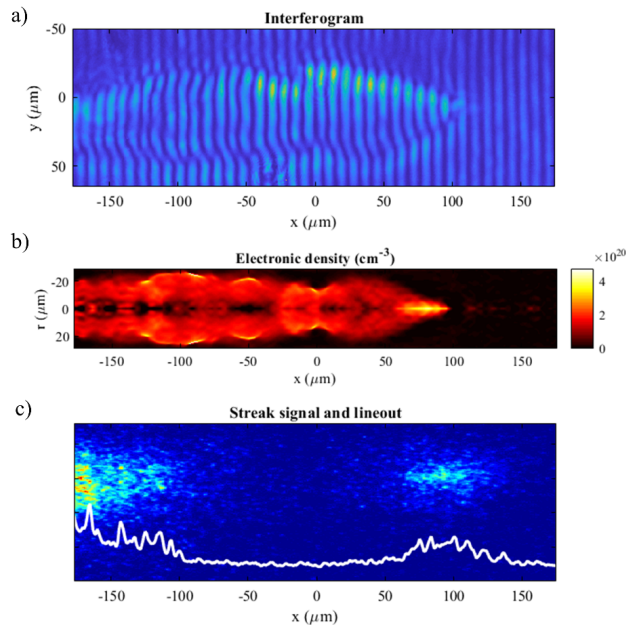


Figure 3. Optical plasma diagnostics show strong self emission from dense narrow regions of the plasma. We see (a) raw interferogram measurement of the plasma, 1 ns after the interaction starts, measured with the Nomarsky interferometer (b) the retrieved electronic density of the plasma and (c) the raw streak camera measurement of the self emission of the same laser shot (including measurement lineout in white).  $x = 0, y = 0$  are the coordinates of the jet shock point; the laser travels left to right and focalizes in the same point.

### III. EXPERIMENTAL RESULTS

For laser shot #63, deploying a pure helium jet, figure 3 illustrates results of optical diagnostics, with 3 (a) the raw interferometric data, 3 (b) the electronic density map and 3 (c) the streaked self-emission of the plasma created in the same laser shot. As expected, taking into account that the interferometry measurement is made 1 ns after the interaction, the plasma has been able to expand and the average density is a fraction of the critical density,  $\approx 0.1n_c$ . The plasma is fully ionized, the retrieved electron number density at the end of the plasma channel is twice as high as the un-driven gas density at the same position for shot #63. The plasma self-emission signal appears frozen in 3 (a), meaning that its duration is much shorter than the resolution of the streak with a 2 ns streak window.

In figure 4 (bottom row) the lineout of the signal of the self-emission of the plasma is overlaid to a picture of

the raw data of the interferometer. The scaled line-out of the self-emission, with position indicated in 3 (a), is visible as white line in 3 (c). This data clearly shows that the laser goes through the peak of the density profile and deposits energy downstream.

**First study** Laser shots #62, #63 and #64 correspond to different gas jet density profiles, as shown in figure 4 (top row), obtained for different gate opening times of the gas reservoir. Note that the backing pressure of 400 bar was constant throughout the experiment. One observes a plateau like feature in the density profile on the left hand side, right before the density peak, see Fig. 4 (#62, top row). The position of the plateau and the location of the self emission peak coincide for shot #62. The plateau density rises in shot #63 and evolves to become part of the rising edge of the peak for shot #64. Thus, for this series of shots, the laser has to traverse a rising areal density of gas before reaching the peak. There, a second self emission zone appears in vicinity of the end of the plasma channel. Comparing Fig. 4 (top row) and Fig. 4 (bottom row), we observe that the first self emission peak corresponds to a initial atomic density of  $1.2 \times 10^{20} \text{ cm}^{-3}$  to  $1.6 \times 10^{20} \text{ cm}^{-3}$ .

Dose converted RCF data is shown in figure 5 for these 3 shots, laser photons and particles propagate out of the sketch plane. One sees active layer imprints over the full RCF stack, layers are numbered in ascending order in direction of particle propagation. A beam-like feature with similar divergence and amplitude is clearly pronounced in all shots. The average FWHM divergence of the beam is  $9^\circ$ . The presumed laser axis according to pre-alignment coincides with the centre of depicted frames for shots #62 and #63, its position is not superposed with the maximum measured dose deposition. This may be due to a alignment error, the RCF stack is not thick enough to confidently determine the particle beam trajectory.

The deposited dose decreases slowly throughout the stack. This does not resemble a dose-depth curve expected for high energy electrons<sup>57</sup>, which would have a peak dose within the stack followed by a steep decay. We derive ion number densities per pixel following a standard protocol established in<sup>51</sup>, presuming alpha particle projectiles, a beam cut-off directly after the last layer of the stack and a step-wise flat spectral shape between two active layers. Note that the number densities in figure 5 are relative to one pixel, with scanner resolution of 600 dpi.

With no further diagnostic of the background signal issued by high energy electrons and photons, we presume the signal of an alpha particle beam with small angular divergence superposed to a broad background. Number density maps are fitted with the sum of two 2D-Gaussian functions for the particle beam, superposed with a second order polynomial in both x- and y-dimension representing the background signal. Fits do not converge without a weighting of the data: after visual centering of the peak signal on a fit-canvas, the uncertainty of pixels is linearly and concentrically increased from 100% at the peak to

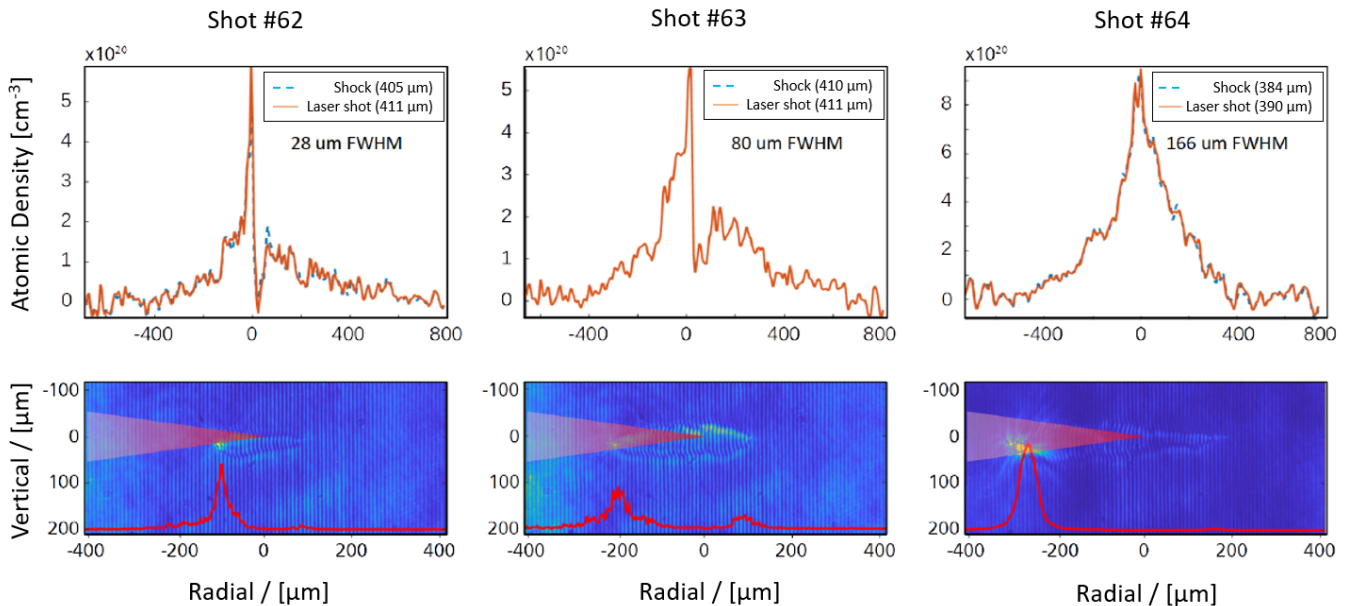


Figure 4. For three consecutive shots varying the pure Helium gas jet density profile, (top row) longitudinal un-driven gas jet density profile, (bottom row) interferometric image superposed to aligned laser beam and plasma self-emission in arbitrary units as red line. The laser is focused to  $x = 0, y = 0$ , the coordinates of the jet maximum density point.

167% in the corners. No further adjustment is done. The integrated particle number within both Gaussians is plotted in figure 6.

The alpha particle spectrum has a peaked shape with following exponential decay. Note that the increase at the end of the spectrum is artificial due to the assumption of a cut-off energy of 42 MeV, yielding an overestimation of the number density influenced by all higher energy projectiles that may have been present. The spectra for shots #62 and #63 are similar in the range of their error. The number density maximum of  $2 \times 10^8 \text{ MeV}^{-1}$  to  $3 \times 10^8 \text{ MeV}^{-1}$  is attained for 22(2) MeV alpha particles. Note that both shots have comparable neutral gas density peaks. Shot #64, with higher gas density peak, shows a thoroughly lower particle number density and the spectral peak at lower energy.  $8 \times 10^7 \text{ MeV}^{-1}$  are attained for 16(2) MeV alpha particles.

In order to better work out the difference in the origin of the different spectra, we turn to the ToF detector results. The deconvolved spectra obtained for the transversely oriented photodiode B assuming alpha projectiles is plotted in figure 7 (top panel).

Note that the longitudinal profile for the un-driven gas jet, the interferometric image of the driven plasma and the plasma self emission are similar for the pairs of shots #61 – #62 and #64 – #66. For smaller volumes of plasma and lower self-emission amplitude in #61 – #62, the particle number and high energy cut-off of the transversely accelerated particles are higher than for larger volumes of plasma and higher self-emission amplitude in #64 – #66. The decrease of particle number and the shift of spectral features to lower energies, here detected in

a direction practically perpendicular to the intense laser axis, aligns with the forward accelerated spectra retrieved with RCF.

The ToF spectra for alpha particles accelerated under a small angle from the laser forward direction are shown in Fig. 7 (bottom panel). The deployed RCF stack in shots #62 and #64 acts as a high-pass filter and cuts off energies below 44 MeV. Overall, alignment precision of the recesses holding the RCF was not well enough monitored to exclude possible clipping of the direct line between laser-focus and ToF photodiode A. Results have to be understood as a lower limit to the unperturbed projectile energy. Therefore, the below limit for the highest recorded projectile energy calculates to 55 MeV for alpha particles.

**Second study** A second study aims at the influence of the transverse laser focus position with respect to the gas jet density maximum. We deploy a gas mixture of Nitrogen and Helium in a 9 to 1 molecular density ratio. The gas jet density was not deliberately altered, but changed with the progressive destruction of the nozzle on a shot-to-shot basis.

Damages were noticed visually with the nozzle viewing system, see figure 8, and due to alteration of the un-driven gas jet density profile. From gas profiles in figures 13 (top row) and 9 (b), we infer likely nozzle damage by laser shots #79 and #81. Interferometric data in figure 9 (a) shows a particularly long plasma channel even though the laser was focused far from the largest areal density in vicinity of the supposed gas density peak. This hints severe damage to the nozzle that destroyed the cylindrical

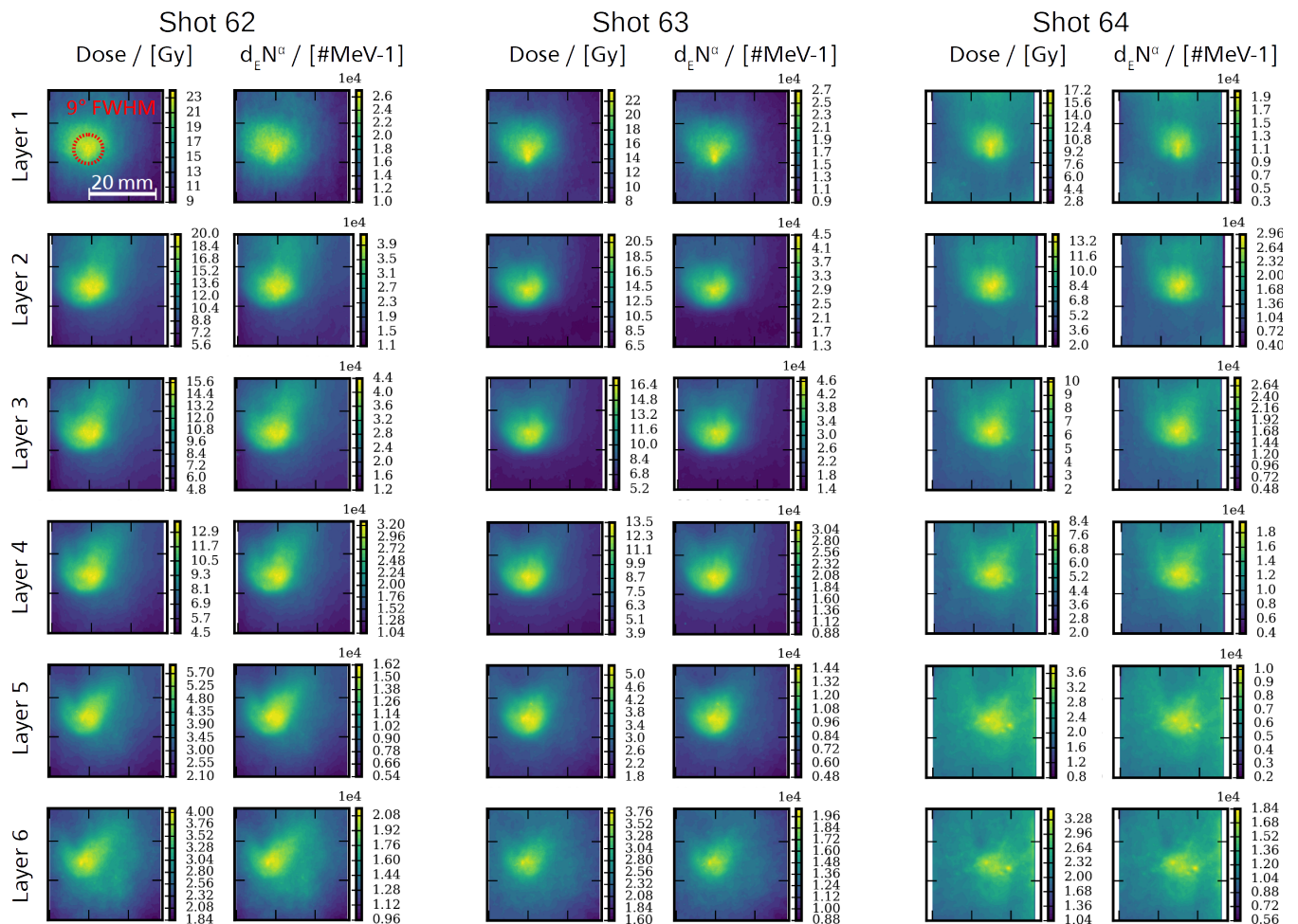


Figure 5. RCF imprints converted to dose and alpha particle number density for three consecutive shots varying the gas jet density profile. The number density conversion presumes the appearance of alpha particles, a cut-off energy equal to the last signal layer and a step-wise flat spectral shape between layers. The typical FWHM divergence angle of the beam imprint is 9°, all images have the same spatial scale. Note that number densities are normalized to one pixel, with respect to the resolution of RCF scans of 600 dpi. For shots #62 and #63, the presumed pre-aligned laser axis corresponds to the centre of the illustrated frames. For shot #64 this does not apply.

symmetry of the gas jet with shot #82. Areal density and peak density of the gas target are thoroughly lower than in the previous study.

A first qualitative view on the RCF data for shots #79, #85 and #87 with displacement of the nozzle of 0  $\mu\text{m}$ , -50  $\mu\text{m}$  and 50  $\mu\text{m}$  respectively, transversely to the main laser axis is given in figure 10. For display purpose, data is averaged over the three color channels. The related energies of both possible species correspond to impact energies of ions with a Bragg-peak in the centre of the active layer.

The laser axis evaluated upon alignment at air pressure is indicated with a white and red crossed marker, it's size represents the alignment uncertainty in air pressure. Photons and particles propagate out of the image plane. Three features are repetitive and clearly pronounced in all shots. Firstly a small spot like peak appears aside the aligned laser axis. Its FWHM half-opening angle is

3°, and it is located at approximately 5 mm right of the supposed laser axis and about 1 mm underneath the horizontal plane where is the laser focus. The sharp peak fades quickly from first to second layer imprint and is only roughly visible in the third layer. The fourth layer does not allow to distinguish the feature. Second, a wide Gaussian peak fills the entire RCF. The FWHM half-opening angle is 11°, the maximum position is superposing the laser axis. The Gaussian is visible throughout the RCF stack, from first to last layer. Third, five lobes appear to be clearly visible on the last layers. One appreciates two maxima and three minima. Both maxima are horizontally aligned next to each other, two minima correspond to these maxima aligned vertically above them. A third minima can be found in proximity of the laser axis, highlighted on the last layer of shot #87 with a white arrow. Two more features appear on the first layer, also highlighted by white arrows. For shot #87 there is

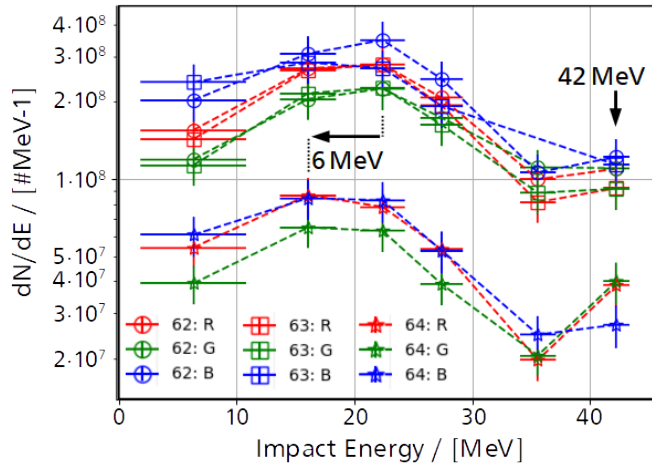


Figure 6. Projectile spectrum for three consecutive shots varying the gas jet density profile, presuming an alpha particle beam impacting on the stack of RCF. RCF color channels R, G and B are independently analyzed.

a shadow visible that demarcates a clear cut from a region of high dose to a region of lower dose. For shot #79, there is a faint maximum visible at the bottom right corner of the film.

On the first four layers, the area between dose signals of different shots on the same RCF layer shows no exposure to dose, whereas both last layers of different RCF type detect dose in these areas and show overall higher doses than the first layers. This indicates that the films used during the experimental campaign where exposed to certain conditions, after their calibration and prior to the experiment, that could have change their response to dose-deposition with respect to the calibrated response. Other than for the analysis concerning shots with pure Helium jets, we are restraint to the last layer imprints and will regard only the first four layers of the stack. Note, that the wide Gaussian could represent an alpha particle beam, with a similar divergence ( $11^\circ$ ) as observed in the first study ( $9^\circ$ ).

Lobe features are fainting barely between third and fourth layer imprint for all color channels, therefore we will assume the fourth layer to be indicative for the background dose delivered by high energy photons and relativistic electrons. For further steps, it is subtracted as background from all other layers.

The spot like beam feature with low angular divergence shows a steeply decreasing dose throughout the stack. This opens the possibility for either electron or ion projectiles, where possible electron beams could have their maximum dose deposition within the detector filter.

Presuming alpha particle projectiles as favoured accelerated ion species due to their lower mass, the signal is fitted to a 2D-Gaussian superposed with a second order polynomial representing remaining background, as before. An example result is plotted in figure 11.

We see the three color channels of the number den-

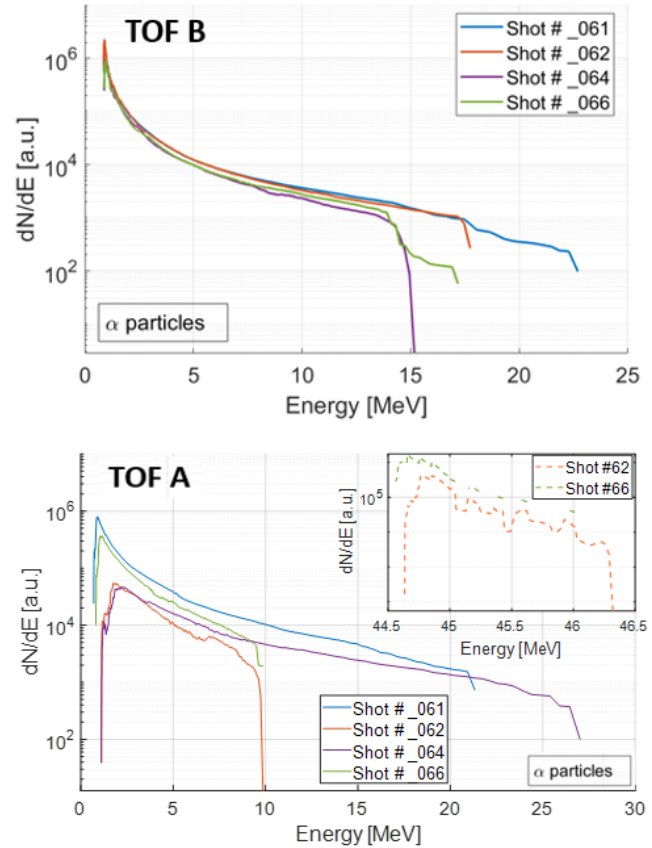


Figure 7. ToF results presuming alpha particle acceleration yield similar spectra in transverse direction (photodiode B, top panel) when comparing shots with similar plasma and self emission characteristics, here for pairs #61 – #62 and #64 – #66. With results obtained under a small angle in laser-forward direction (photodiode A, bottom panel) we see the influence of the passive particle detector present for shots #62 and #64 that acts as a thick filter with low energy cut-off of 44 MeV. Ions stopping over the "filter" shift the maximum detected energy down to  $\approx 10$  MeV in the case of shots #62 and #66. Inset shows spectra of shots #62 and #66 considering the attenuation in the RCF stack, see details of the stack composition in Section II.

sity transformed data in the upper left corners of each sub-plot. The upper right corner displays the best fit result, which is then separated into background in the lower right corner and peak in the lower left corner of the plot panel. We appreciate a low level background signal that is close to a linear evolution, fainting from left to right and bottom to top. The dashed white lines intersect on the laser axis. The background is not symmetric with respect to the laser axis. The Gaussian fit allows to retrieve the total amount of particles per energy by integration over the full beam. Results are shown in figure 12, points with large uncertainties need a critical interpretation, they mostly are of fits on data dominated by the background signal.

The total particle number spectra are flat over the

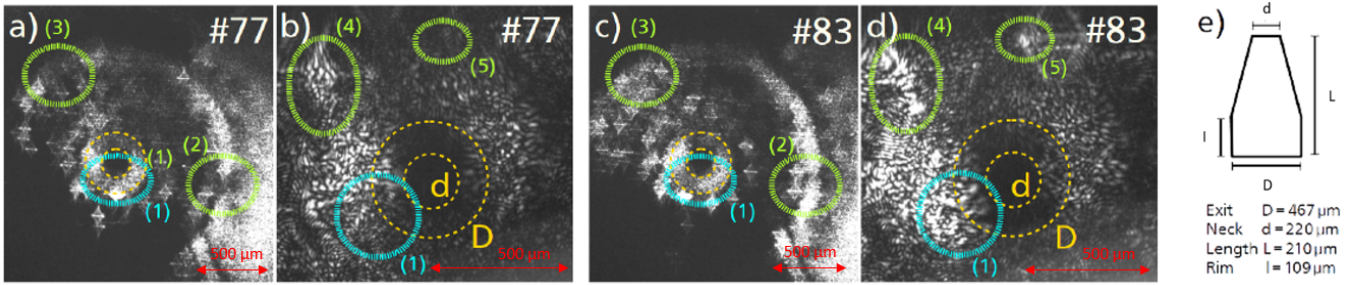


Figure 8. The shock nozzle deployed for the series of shots #77 to #87 shows visual changes after some laser shots. The bottom view image of the original nozzle (a) and a magnified image (b) before shot #77 are compared to the respective images taken before shot #83 in (c) and (d). The shock nozzle geometry (e) is initially cylindrical symmetric and mechanical changes to the shape and the surface quality impact the gas flow. Note visual changes in (a–d) with highlighted areas (1–5), of which (1), in blue, affects directly the nozzle cone (exit and neck diameter are indicated with yellow dashed lines).

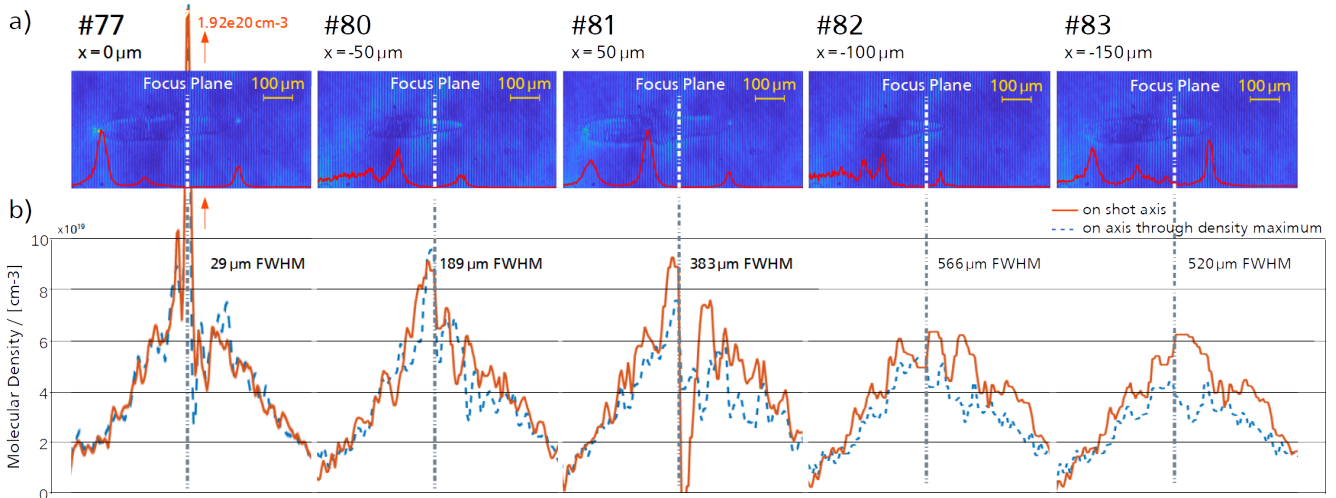


Figure 9. (a) Interferometric images overlaid by self-emission line-outs for shots with variation of the transverse position of the laser-gas interaction. The longest plasma channel is recorded for shot #81 with positive transverse displacement – the length of the channel decreases for the series of shots towards negative transverse displacements. The last shot of the series #83 does not agree with this assessment and shows a longer channel again. Note that (b) un-driven gas density profiles acquired prior to corresponding shots show visual changes from shot-to-shot, indicating changes to the nozzle. This agrees with a qualitative difference of the nozzle surface between shot #77 and #83, presented with fig. 8.

large energy range from 6.3 MeV to 22.4 MeV. With an average of  $1 \times 10^7 \text{ MeV}^{-1}$  alpha particles, the beams represent bunches of the order of  $10^8$  ions. The particle number density decreases for increasing particle energies throughout the data. The spread of results for different color channels in one shot and the same layer is of the order of the shot-to-shot variation. Nevertheless, the largest amplitudes in this shot series are consistently recorded for shot #87, the lowest for shot #85.

The molecular density of the gas jet in the respective laser shots is shown in figure 13, aside the on-shot interferograms overlaid by line-outs of the streaked self emission. For small transverse displacements, the first self emission peak corresponds to an un-driven density of  $2 \times 10^{19} \text{ cm}^{-3}$ .

We record lower particle number densities for negative displacement and higher number density for positive

displacement ( $+50 \mu\text{m}$ ) comparing shots #85 and #87. With respect to RCF results, a longer plasma channel and a higher first self-emission peak yield lower particle number densities. The cut-off energy remains the same, but drops underneath the detection limit allowing a confident fitting.

Spectra from the ToF signal in this shot series, can be seen in Fig. 14. Alpha particle energies vary from 13 MeV to 24 MeV for the laser forward emission ( $16^\circ$  from the laser axis) and from 16 MeV to 19 MeV for the transverse emission ( $106^\circ$  from the laser axis). Maximum energy cut-offs are less spread in the transverse emission. The number of particles that arrived to the front detector (ToF A) is slightly lower than the number of particles arriving to the transverse detector (ToF B).

The corresponding interferometric results and gas density profiles are shown in figure 9. The bulk gas shows



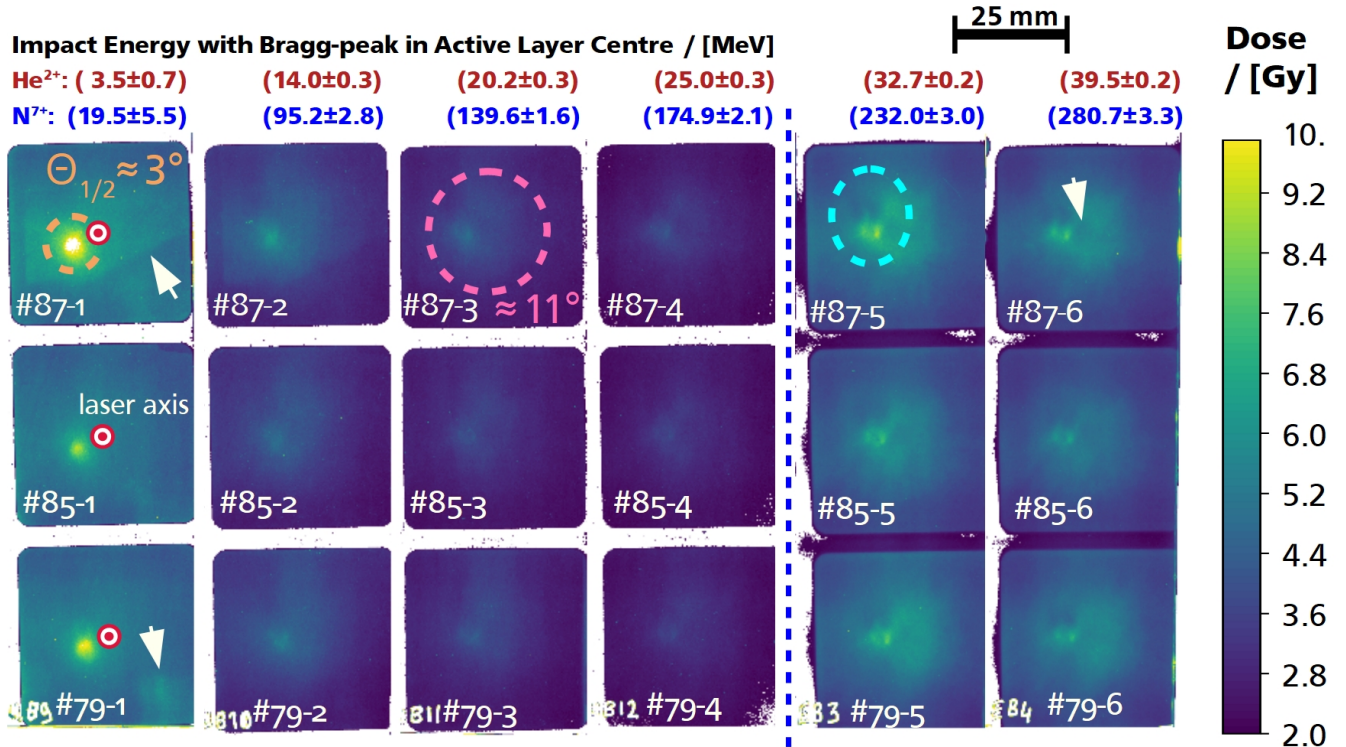


Figure 10. Overview on RCF results for shots #79, #85 and #87 converted from RAW to deposited dose maps.

only small shot-to-shot differences. The first self emission peak moves towards the focus plane for larger transverse displacements, likely to raise at a fixed density as observed in the first study.

The only pair of shots with inter-comparable gas undriven density profiles #80 – #81 shows similar transverse cut-off energies and number densities. However, we encounter a higher cut-off energy in the laser forward direction in shot #80. Alike for shots with RCF detector, shot #80 with shorter plasma channel and more dilute first self-emission peak corresponds to the shot with slightly higher number density in the forward direction.

The transverse displacement of the gas jet with respect to the laser focus and the shot-to-shot damage to the nozzle do only slightly alter the particle beam spectrum. Accelerated particles may come from the interaction in the bulk gas rather than from the density peak.

In order to determine the ion species and resolve the ambiguity of results obtained with RCF and ToF detectors, we deploy CR-39. The chemical etching post-processing unravels clear etch pits on all exposed slaps of CR-39, an indication for the presence of ion species in laser forward direction. The track density map in the vicinity of the laser axis shows a uniform etch pit distribution over all pit sizes. This may correspond to the large Gaussian distributed dose, visible with RCF results.

The spectral range of all results is summarized with in Fig. 15. Ambiguous are indications for ions of either alpha particles or Nitrogen ions, if both species may yield

the same observation. Clear measurements indicate alpha particles of 5 MeV, close to the alpha particles issued by the decay cascade of natural Radon gas, as well as low energy Nitrogen projectiles. Some of the ambiguity may be resolved by taking into account the observed range for ions responsible for the wide Gaussian peak on RCF, with FWHM divergence of around 10° observed in both series of shots discussed herebefore. None of the etch pits of CR-39 interpreted as Nitrogen stems from energies necessary to penetrate the RCF stack up to the last layers. On the contrary, CR-39 results fully cover the range of alpha energies corresponding to RCF imprints.

The consistency of spectral ranges for alpha particles found by RCF and CR-39, indicates them to be the ion species responsible for observed large beam features. The ambiguity for small beam features can not be resolved based on the set of diagnostics employed for this study.

#### IV. PARTICLE-IN-CELL (PIC) SIMULATIONS

1D particle-in-cell (PIC) simulations have been conducted in order to better understand the experimental results and the complex acceleration mechanisms that could have taken place during the interaction. The parallelized PIC code CALDER developed at CEA was used<sup>58</sup>. We discuss here two of the runs.

The simulated density profile was obtained by fitting a wave-front measurement acquired during the experiment.

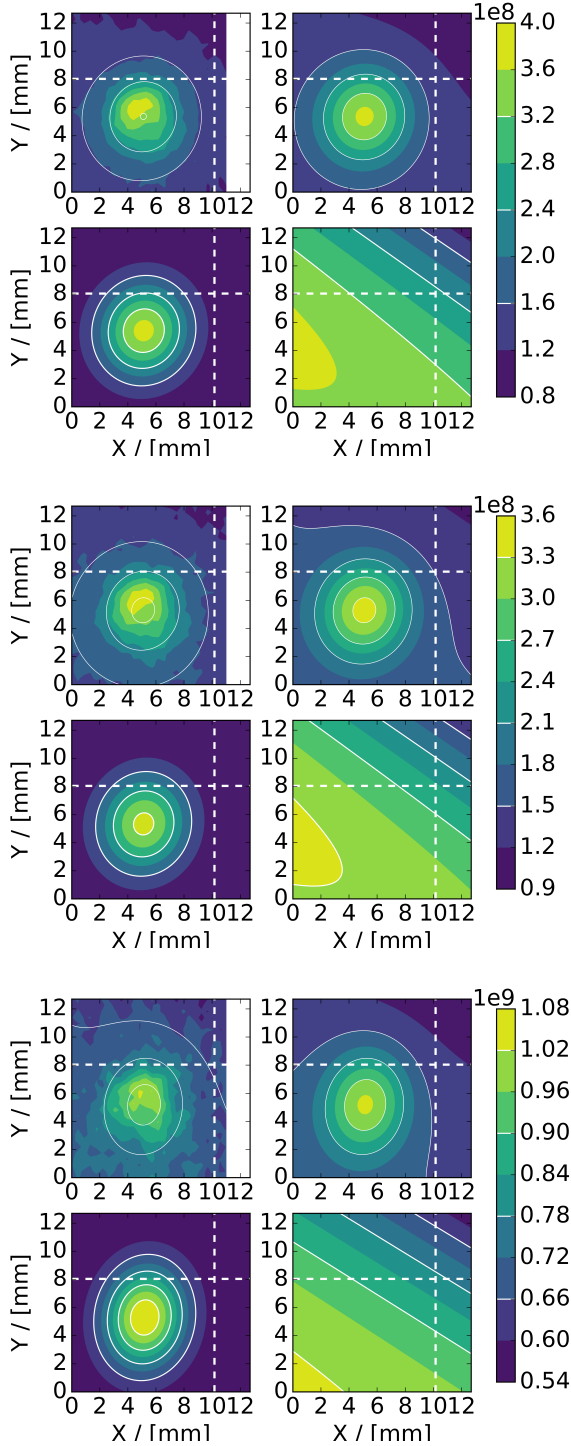


Figure 11. Zoom of the peak visible on the first layer U-EBT-3 for shot 79. Each subplot shows one color channel. Therein, clockwise from the top-left corner, (1) the data, (2) a second order polynomial background and a two dimensional gaussian fitted to the data, (3) the gaussian in isolated view and (4) the background isolated. The horizontal plane is parallel to the x-axis and the vertical plane parallel to the y-axis. The color bar is indicative to allow comparison of the four subplots with each other. The intersection of white dashed lines indicate the pre-aligned laser axis position.

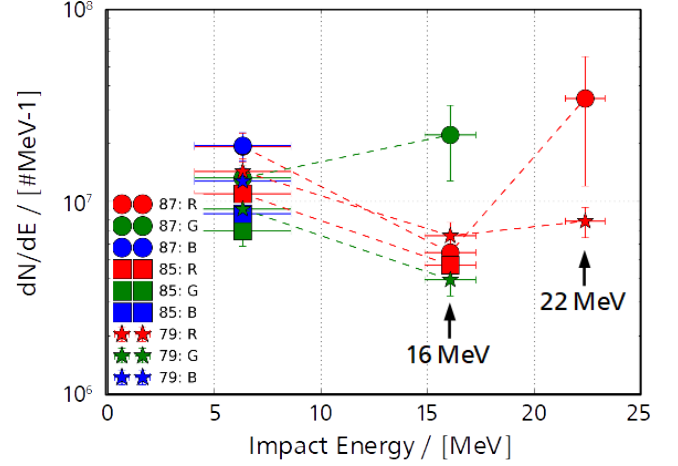


Figure 12. Projectile spectrum for three consecutive shots varying the gas jet density profile and transverse position, presuming an alpha particle beam impacting on the stack of RCF. RCF color channels R, G and B are independently analyzed.

Since the experimental data presents a lot of fluctuations, likely due to the acquisition diagnostic, a double exponential function was fitted to a gaussian smoothing of the data using a resolution of  $0.5 \mu\text{m}$ . The exponential fit was extrapolated until the minimum density of  $10^{18} \text{cm}^{-3}$ . The latter was chosen sufficiently low in order to avoid strong non-physical TNSA that would otherwise appear at the wings of the profile due to a primary interaction of the laser with an initial high target density. Both the density profile and the corresponding exponential fit are plotted in Fig. 1 (e).

In the following, and unless explicitly marked differently, the density, velocity, time, distance, mass, electron impulsion, ion impulsion, energy and electric field are normalized to the following quantities, respectively:

$$n_c, c, \omega_0^{-1}, c/\omega_0, m_e, m_e c, m_i c, m_e c^2, m_e \omega_0 c/e, \quad (1)$$

where  $\lambda_0$  is taken to be equal to  $1 \mu\text{m}$ ,  $n_c$  is the critical density for a  $1 \mu\text{m}$  laser wavelength equal to  $1.11 \times 10^{27} \text{m}^{-3}$ ,  $c$  is the velocity of light,  $\omega_0^{-1}$  is the corresponding inverse laser frequency equal to  $5.31 \times 10^{-16} \text{s}$ , and  $m_e$  and  $m_i$  are the electron and the ion rest masses, respectively.

The main physical inputs of the simulations were a 1D geometry due to the mm spatial scales run over 10 ps, and the impact and field induced ionization of the initially neutral gaseous target, composed by 90% atomic nitrogen and 10% helium. Coulomb collisions between all charged particles were considered. Absorbing boundary conditions were used for fields and particles. Each cell of initially neutral Nitrogen and Helium atoms contained 100 particles, while the electrons were created by the ionization processes. The initial ion temperature was  $T_i = 1 \text{eV}$ . The temporal and spatial resolutions were

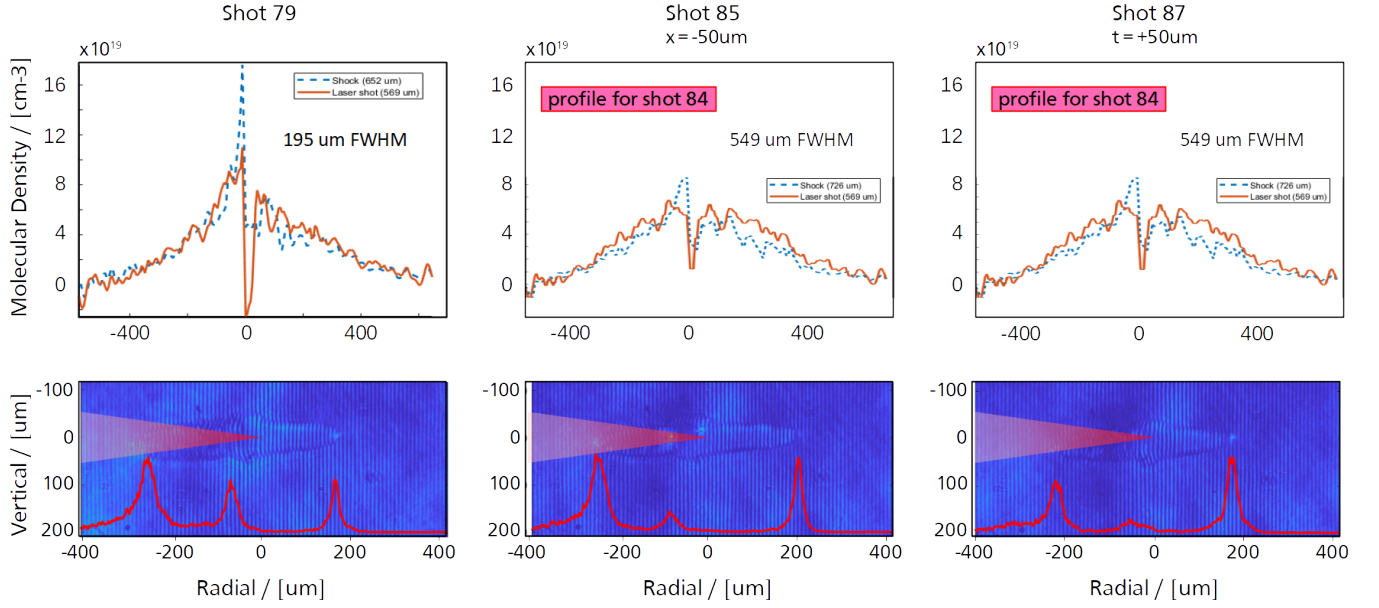


Figure 13. Shot-to-shot variation of the gas jet density profile using a mix of Helium and Nitrogen in a ratio 1 to 9, (top row) longitudinal un-driven gas jet density profile, and (bottom row) interferometric image superposed to aligned laser beam and plasma self-emission in arbitrary units as red line, 1 ns after the interaction starts. The laser is focused to  $x = 0, y = 0$ , the coordinates of the jet shock point, but transverse displaced by  $0 \mu\text{m}$  and  $\pm 50 \mu\text{m}$ .

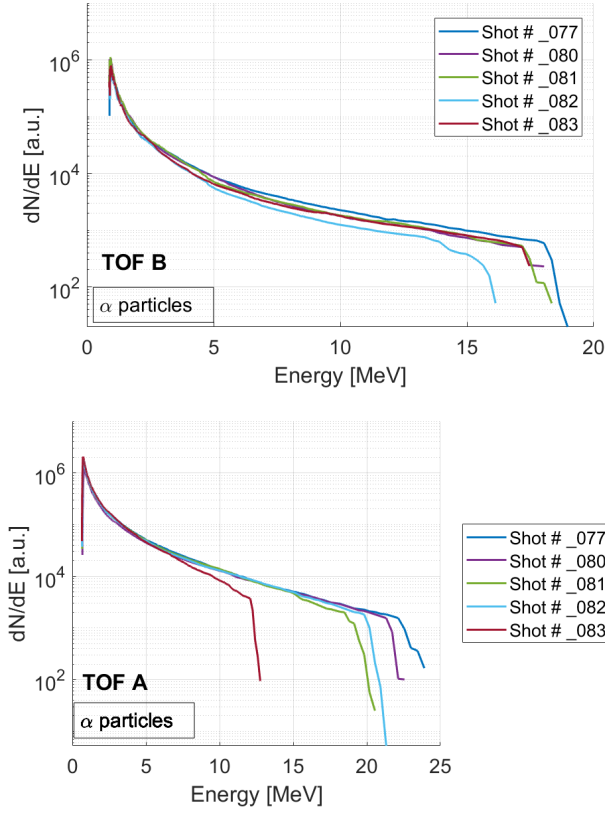


Figure 14. Spectra obtained after the analysis of the time-of-flight A (top) and B (bottom) signals assuming alpha particles acceleration for five different shots.

0.05 fs and  $0.016 \mu\text{m}$ , respectively.

The first simulation that was performed shows the interaction of a laser pulse characterized by a normalized laser amplitude  $a_0 = 6.8$  (peak intensity  $I_L = 10^{20} \text{ W/cm}^2$ ), a wavelength  $\lambda_L = 0.8 \mu\text{m}$  and a pulse FWHM duration  $\tau_L = 30 \text{ fs}$  (VEGA II laser pulse characteristics) interacting with the density profile plotted in Fig. 1 (e), reaching a maximum atomic density  $n_{at,max} = 4 \times 10^{20} \text{ cm}^{-3}$  ( $0.36 n_c$ ). The laser is linearly polarized along the  $y$ -axis and is injected from the left-side of the simulation box.

Premature laser absorption and reflection in the up-ramp of the gas target (before  $x = 1000 \mu\text{m}$ ) was observed as seen in the  $E_y$  field chart in Fig.16. Density peak at  $x = 1306 \mu\text{m}$  is indicated by the vertical dashed line.

On the final time step of the simulation the ion phase spaces of both Nitrogen ions and alpha particles were very similar: the Nitrogen ions phase space can be seen in Fig. 17. Non-linear ion acoustic waves develop in both up and down density ramps after the laser has crossed. These ion waves depart from a single point into symmetrical, opposite directions, moving as expected at a velocity close to the ion sound speed  $c_s$ . At some point during their trajectories, reflection of background ions occurs. The reflection in the direction of propagation of the wave is privileged.

The resultant ion energies in the laser propagation direction are ten times lower than those measured experimentally. One of the possible reasons for this discrepancy is that due to a laser pointing error the laser could have

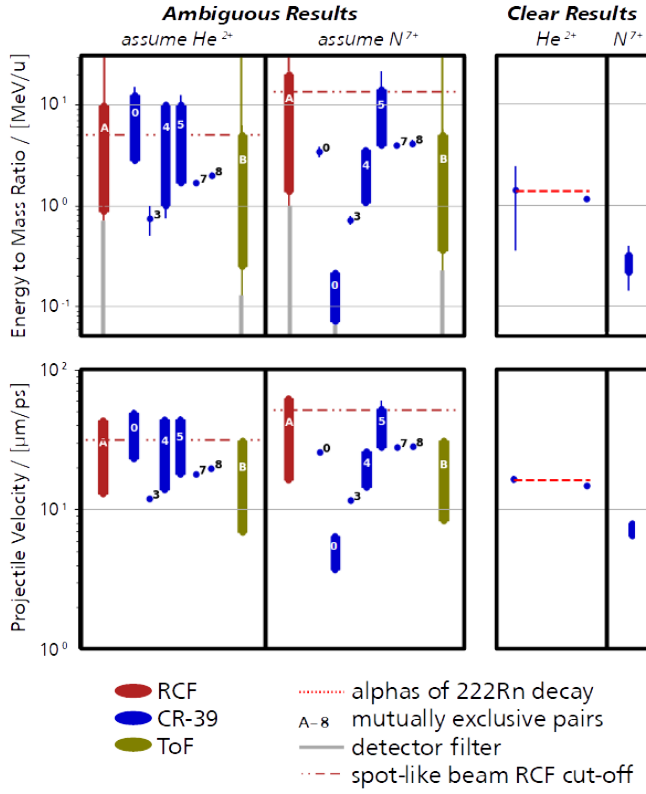
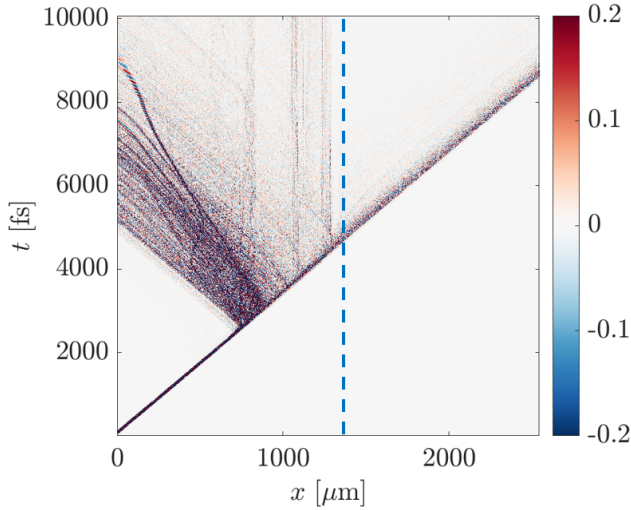
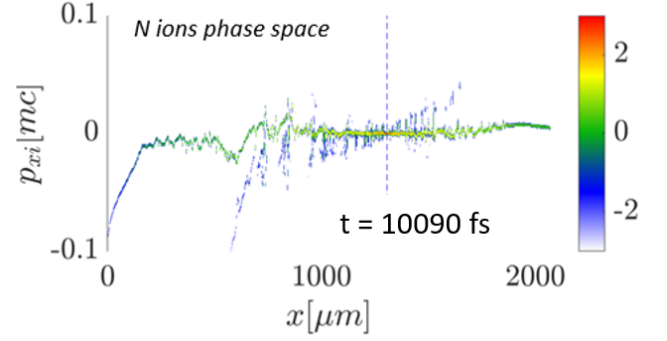


Figure 15. Summary of results.

Figure 16.  $E_y$  field chart resulting from the simulation with a density profile with  $n_{at,max} = 4 \times 10^{20} \text{ cm}^{-3}$ . The blue dashed line marks the density peak.

interacted with a less dense target region located on the wings of the profile. The gas target could have also pre-expanded due to the interaction of a  $\approx 5$  ps-long intensity ramp with a maximum intensity of  $10^{10} \text{ W/cm}^2$ , that was systematically seen in the laser pulse contrast measurements performed during the experimental campaign (see

Figure 17. Nitrogen ion phase space in the last time step of the simulation with a density profile characterized by a  $n_{at,max} = 4 \times 10^{20} \text{ cm}^{-3}$ .

inset in Fig. 2).

The laser is expected to have crossed the profile's density peak as can be assumed by looking at the interferograms of figures 4,9 and 13, where a plasma channel traverses the peak. Therefore, a second PIC simulation with the maximum density reduced by a factor 10 and a slightly increased  $a_0 = 8$  was conducted. The maximum experimentally measured  $a_0$  was 7.4. The slight increase in the laser intensity could reproduce the effect of laser self-focusing, absent in 1D simulations.

The ion acceleration processes are different in the conditions of the second simulation. The main mechanism seems to be CSA developed from strong electron pressure gradients in the density peak as illustrated by the electron phase space of Fig. 20, top graph. TNSA (amplified by the profiles abrupt unrealistic density cut) is also seen in the extremes of the density profile in Fig. 21 at  $x < 200 \mu\text{m}$  and  $x > 2400 \mu\text{m}$ . As has been previously studied<sup>20</sup>, the electronic temperature chart in Fig. 19 shows that near-critical interaction entails volumetric heating up to relativistic temperatures (normalized  $T_e \approx a_0$ ) through wavebreaking of the electron plasma wakefield and phase mixing between trapped and return-current electrons. Once the laser crosses the density peak the electrons are reflected by the charge separation field created in the down-ramp. An initial single electron vortex located at the density peak and confined by the shock electrostatic barriers evolves into two separate electrostatic structures that descend through both the up and down density ramps of the profile, triggering ion acceleration up to  $v_i = 0.05c$ , as seen in figure 20. By  $t = 8070$  fs the shock borders are located at  $1200 \mu\text{m}$  and  $1400 \mu\text{m}$ . The accelerated ion velocity profile continually steepens while moving down the target ramps and reflects background ions if the correct shock reflection conditions are achieved. Locating ourselves in the frame of the shock, reflection will be produced when the kinetic energy of the incoming particles is higher than the electrostatic potential of the shock barrier. If the ions kinetic energy is lower than the potential they will cross the shock region

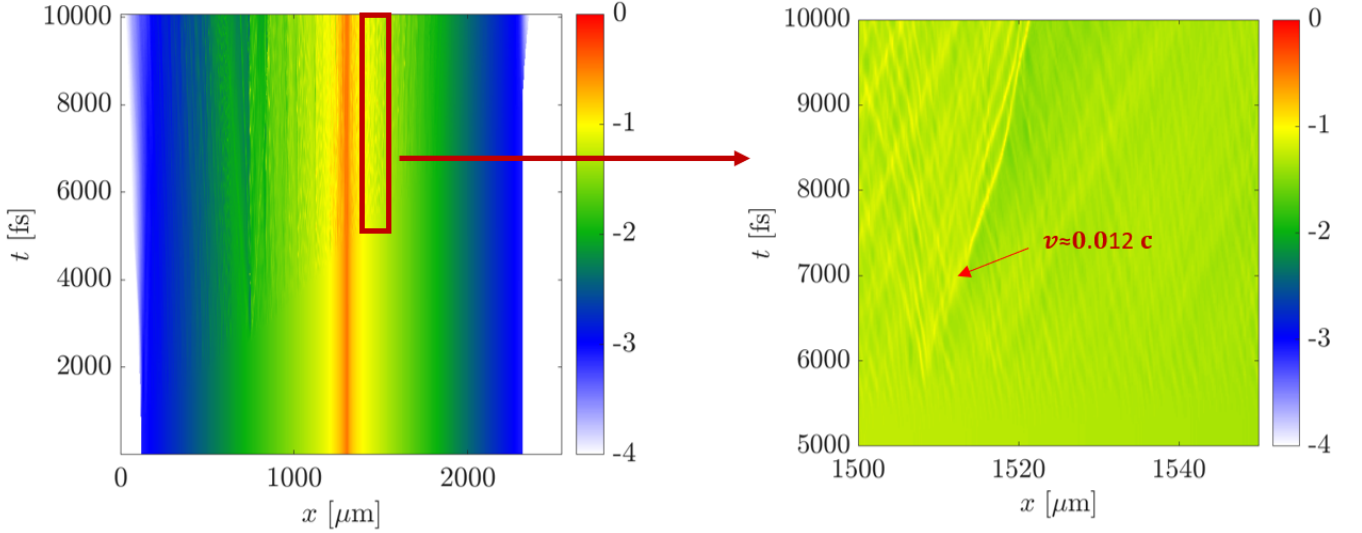


Figure 18. Nitrogen ions density chart (left) and zoom on one of the ion acoustic waves travelling in the down-ramp of the density profile (right) for the first simulation run with  $a_0 = 6.8$ .

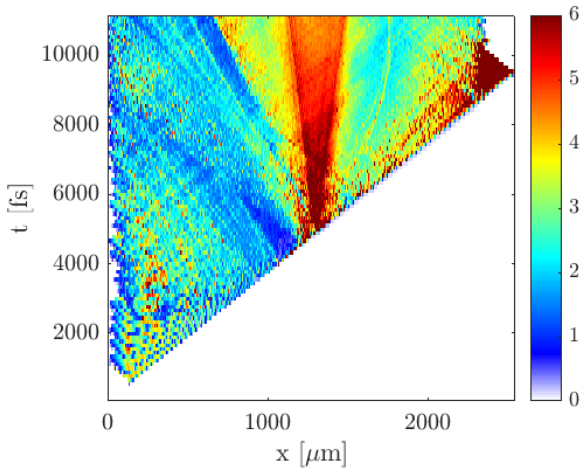


Figure 19. Electronic temperature chart in MeV of the  $n_{at,max} = 4 \times 10^{19} \text{ cm}^{-3}$  ( $0.036 n_c$ ) simulation.

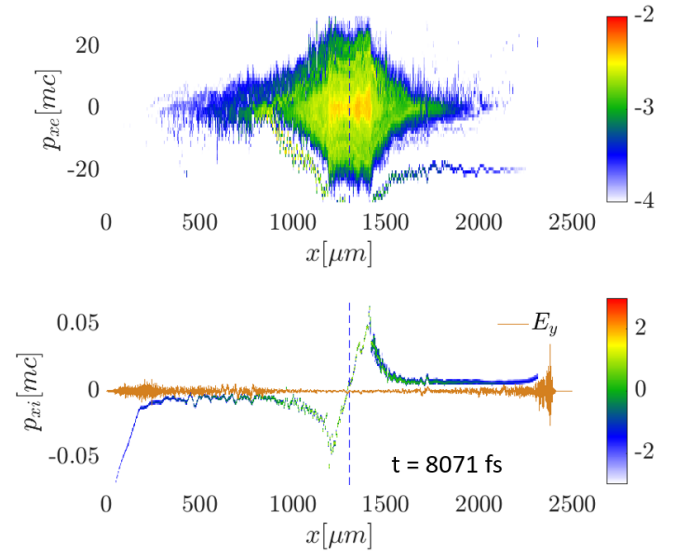


Figure 20. Electrons (top) and nitrogen ions (bottom) phase spaces after the laser has crossed the density peak and traversed the density down-ramp.

and suffer deceleration in the process. By the end of the simulation (see ion phase space of figure 21) the reflected ions have been accelerated up to velocities  $v_i = 0.15c$  equivalent to ion energies of  $\epsilon_\alpha = 40 \text{ MeV}$  and  $\epsilon_N = 150 \text{ MeV}$ . These values are in agreement with the experimentally measured ones. The perturbation in the ion phase space seen at  $x = 1800 \mu\text{m}$  is the result the evolution of an initial resonance between the laser frequency and the plasma ( $\omega_L = \omega_{pe}$ ) at  $x \approx 1320 \mu\text{m}$  immediately after the laser crosses the density peak ( $t = 4630 \text{ fs}$ ).

## V. CONCLUSION

In this experiment we have demonstrated the effective acceleration of broad-spectrum Helium ions beams with cut-off energies above 25 MeV and peaked ion number density  $10^8 \text{ MeV}^{-1}$ , resulting from the interaction of ultrashort ultraintense laser pulses with near-critical plasmas generated by high pressure gaseous shocked jets. Moreover, this kind of gas jet is capable of delivering the target at HHR, following the available repetition rate of the new generation of high intensity Ti:Sa laser systems

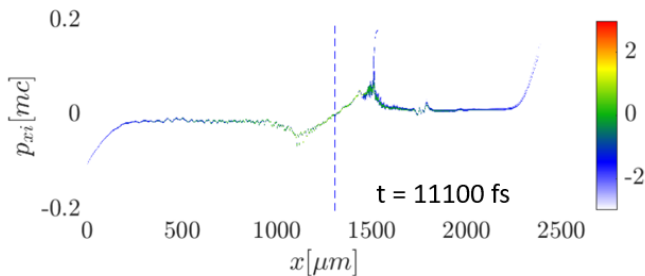


Figure 21. Nitrogen ions phase spaces at the last time step of the simulation with  $n_{at,max} = 4 \times 10^{19} \text{ cm}^{-3}$  ( $0.036 n_c$ ).

(1-10 Hz), yielding therefore an enhanced time-averaged flux of accelerated particles, necessary for most of the medical and industrial applications, such as radiopharmacy. Most of the applications would exploit the unique properties of the laser-driven ion beams (high density, ultra-low emittance, compactness), which may greatly surpass those attained on more costly and larger-scale radiofrequency accelerators.

The acceleration from the shocked gas jet target shows repetitive results even for small variations in the gas jet profile. The advent of sub- $\mu\text{m}$  high precision 3D-printing of mesostructure ceramics<sup>59</sup> may be beneficial to mass-produce more robust and more precisely tailored shock nozzles. Note that efforts towards automatized nozzle exchange systems and good vacuum systems remain non-trivial technical challenges. Other technical difficulty towards HRR operation of the acceleration platform concerns the vacuum pressuring capability and the strategies to protect the facility compression optics in case of hazardous gas leakages.

A PIC simulation of the interaction of an  $a_0 = 6.8$ ,  $\tau_L = 30 \text{ fs}$ ,  $\lambda_L = 0.8 \mu\text{m}$  laser pulse (VEGA II characteristics) with a density profile extracted from experimental measurements (with  $n_{at,max} = 4 \times 10^{20} \text{ W/cm}^2$ ,  $0.36 n_c$ ) was performed. Premature laser absorption in the density up-ramp inhibited strong particle acceleration. The accelerated ion energies were 10 times lower than the ones measured experimentally. Ions were accelerated by reflection from IAW developed both in the up and down density ramps of the profile. Since the laser is seen crossing the density peak in the on-shot interferograms, a second simulation with a factor 10 reduction of the density ( $n_{at,max} = 4 \times 10^{19} \text{ cm}^{-3}$ ,  $0.036 n_c$ ) was performed, with the intention of simulating conditions that resemble what was experimentally seen. An slight increase in  $a_0$  from 6.8 to 8 (the highest experimentally measured  $a_0$  was 7.4) was also included in the second run. An increasing  $a_0$  is a standard effect of laser self-focusing which is absent in 1D simulations. In this case, ion acceleration through collisionless shock formation having its origin in strong electron pressure gradients located in the density peak was observed. TNSA acceleration was also seen in the target extremes. Strong electron heating up to  $T_e \approx a_0$  was obtained. The final reflected ion velocities

are in agreement with the experimental measurements.

## VI. FORESEEN APPLICATIONS

Generalizing to the laser repetition rate, the alpha particle beam demonstrated in this study has a beam-current of  $64 \text{ pA Hz}^{-1} \text{ MeV}^{-1}$ . Such beam currents are of interest in radio-chemistry. Radiolysis, the breaking of chemical bonds by radiation, is conducted with alpha projectiles with tens of MeV<sup>60</sup> and beam currents of 10 nA to 100 nA – parameters that can be achieved even with low repetition rate. Further optimization of the platform is of interest regarding short ion bunches for picosecond pulse radiolysis research<sup>61</sup> and may yield to high brilliance sources for not time averaged observations conducted with single shots<sup>62</sup>.

Alpha therapy is a promising approach for clinical oncology, promoting the targeted destruction of a cancerous tumor and metastases in vivo<sup>63</sup>. This form of radiotherapy is not carried out by external radiation, but by administering radioactive substances to the patient. The cells are reached through the bloodstream. Unlike chemotherapy, the treatment is aimed at diseased cells due to the targeted binding properties of compound molecules and thus reduces possible side effects<sup>64</sup>. Alpha-emitting radionuclides can be produced by interaction of ionizing radiation with a suited target material, which is a major challenge for reasons of the needed quantities<sup>63</sup>. Astatine-211 is a suited candidate for its intermediate half live time of 7.2h and low risk for side effects<sup>65</sup>, which can be produced in a  $(\alpha, 2n)$  reaction by irradiating bismuth-209 with alpha particles of 28 MeV. Beam currents of several hundred  $\mu\text{A}$  are necessary for efficient isotope production and therefore repetition rates of the kHz and alpha particle number densities by three orders of magnitude higher than observed – a clear motivation for further studies, where more energetic lasers can play an important role.

## VII. ACKNOWLEDGMENTS

We thank C. Sergeant and Ph. Barberet (CNBG, Univ. Bordeaux, Gradignan) as well as B. Bondon and all the technical staff (UF Chimie, Univ. Bordeaux, Campus Talence), for their unconditional help and the provision of the necessary analysis equipment and expertise for the etching of CR-39.

We would like to thank Ashland Specialty Ingredients G.P., that promptly agreed to help us detecting low doses of narrow-band spectra in the low MeV range by producing a then not available special type of RCF. The unlaminated EBT-3 (U-EBT-3) masters this task with its sensitivity equal to EBT-3 in a thin layout. Many thanks to Jérôme Caron that allowed us to take calibration data for RCF with his support at Institut Bergonié in Bordeaux.

This work has received funding from the European Union's Horizon 2020 research and innovation program under grant agreement no 871124 Laserlab-Europe.

We received financial support from the French State, managed by the French National Research Agency (ANR) in the frame of "the Investments for the future" Programme IdEx Bordeaux – LAPHIA (ANR-10-IDEX-03-02).

We acknowledge the support from the LIGHT S&T Graduate Program (PIA3 Investment for the Future Program, ANR-17-EURE-0027).

We acknowledge GENCI for providing us access to the supercomputer Irene under the grants no. A0070506129 and no. A0080507594.

This project has received funding from: i) the Spanish Ministerio de Economía y Competitividad through the PALMA Grant No. FIS2016-81056-R, ii) the Spanish Ministerio de Ciencia, Innovación y Universidades ICTS Equipment grant No. EQC2018-005230-P, iii) the Laser-Lab Europe V Grant No. 871124 and iv) the Junta de Castilla y León grants No. 659 CLP087U16 and No. CLP263P20.

## VIII. ADDITIONAL MATERIAL: METHODS

### A. Laser Diagnostics

Key to a good focal spot quality was a two translations plus two tilt axis motorization system of the OAP mount allowing for flexible alignment under vacuum. The focal spot was optimized every day at air pressure, yielding a FWHM of  $7.5 \pm 1.4 \mu\text{m}$  with a varying percentage between 20% and 40% in the FWHM.

The pulse duration was verified employing an auto-correlator, yielding  $37.06 \pm 0.81$  fs. The temporal contrast was measured with the commercially available spectral filtering third-order cross-correlator system Sequoia (Amplitude Technologies).

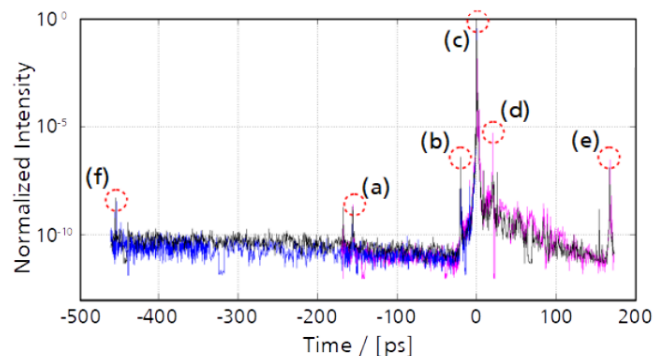


Figure 22. Three independent Sequoia measurements. Identified pre and post-pulses have been marked with a dashed circle.

Three independent Sequoia measurements of the tem-

poral contrast at best compression with a  $10^{-10}$  to  $10^{-11}$  ASE level can be seen in fig. 22. Identified pre- and post-pulses are located at (a)  $-156$  ps due to the pockels cell at the regenerative amplifier, (b,d)  $\pm 20$  ps as likely artifacts of the measurement itself and (e)  $167$  ps due to the pockels cell at the regenerative amplifier. (f) is unidentified, (c) indicates the main pulse.

### B. ToF Analysis from PIN diodes data

PiN diodes and many other Time-of-Flight (ToF) detectors rely on time resolved voltage signal read-out, e.g. by fast oscilloscopes. Projectiles impacting on ToF detectors alter proportionally the detector voltage.

The PiN configuration of the diodes includes an extra neutral layer "I" in the middle of the doped layers "P" and "N", which allows for a quantum efficiency enhancement by increasing the cross-section of ionizing radiation with the diode substrate, and a faster response in absence of a minority carriers current that delays the signal current formation. The temporal resolution is  $4.5$  ns FWHM. With pressurized gas entering the vacuum chamber, the photodiode exhibits another advantage with its bias voltage of  $-60$  V. This is comparatively low to other ToF detectors such as microchannel plates, which are polarized with bias voltages of the order of kV which represent risk of short-circuit currents through the momentarily imperfect vacuum.

The obtained signal includes the photopeak and the accelerated particles contribution. An example of the obtained signal is plotted in figure 23. The photopeak refers to the peaked detector response to photons emitted from the laser-plasma interaction and successive cooling. It is pronounced with a first sharp rising edge of the signal allowing one to retrieve a reference detection time  $t_0$  for photons travelling at the speed of light  $c$ . For the charged particle projectiles, we obtain velocities  $v_p = s/t_p$  corresponding to detection times  $t = t_0 + t_p - s/c$ . Knowing the drifting length  $s$  and assuming a particle mass, one can retrieve an energy spectrum of the accelerated particle species.

In order to distinguish between several possible species, the calculated low energy cut-off can be compared to the cut-off which is defined by the thickness of a filter in front of the detector. Electrons are generally present in laser accelerated species. However, by knowing the filter thickness in front of each photodiode the signals acquired during this campaign can not correspond to electron projectiles. Therefore, the signal outside the photopeak must be attributed to ions being accelerated. In our experiments, these could be Helium and/or Nitrogen ions.

During the campaign there were four shots where no particle acceleration was seen in the detector (due to the nature of that specific shot conditions) and only the x-ray photopeak was acquired. The photopeak signal was found to be almost constant in intensity and decay time from shot-to-shot and to follow an exponential decay with

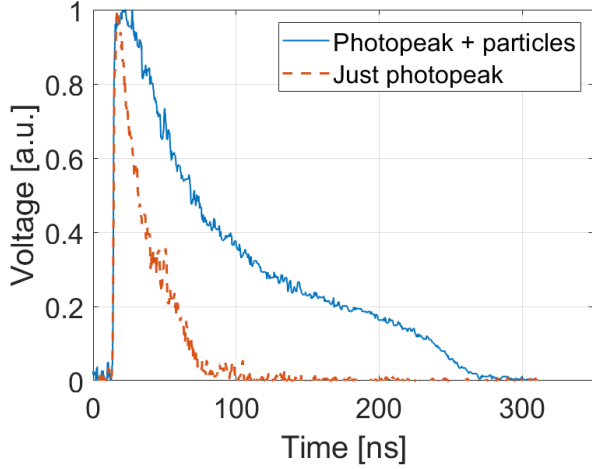


Figure 23. Comparison between the detector RAW signal comprising photopeak and all accelerated particle species (blue full line) and a signal with photopeak only (orange dashed line).

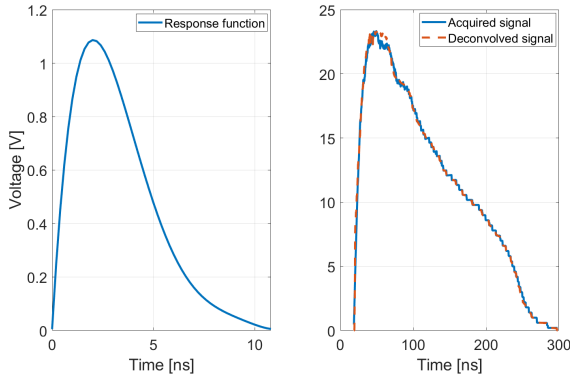


Figure 24. Photodiode detector impulse response (left) and signal after deconvolution (right).

a mean  $\tau$  constant equal to 0.2 ns. Therefore and in order to obtain the ion part of the signal an exponential decay with the mentioned  $\tau$  constant is subtracted from the original signal.

Once the photopeak contribution has been subtracted the original signal must be obtained by performing a deconvolution with the photodiode's impulse response, which is an exponentially modified gaussian. This was characterized in a previous campaign at CLPU by shooting low energy laser pulses (considered as an impulse input signal) directly at the detector. It was seen to be independent from the applied bias voltage. The detectors response function and the deconvolution result can be seen in fig. 24.

To our best knowledge available calibration data<sup>66</sup> is related to X-ray energy deposition with a linear calibration coefficient of  $0.282 \text{ J C}^{-1}$ . However, since the photodiode response can be assumed to be linear if no satura-

tion is produced, the ordinate can be used in a relative manner representing relative number density counts: see Fig. 7 and Fig. 14.

### C. Passive particle Detectors

Both passive detector types, RCF and CR39, are used in alternation and therefore clamped in a fully motorized holder. The casing comprises two plates with a multitude of squared frames of 40 mm sides. The recesses are cut out of 3 mm thick Aluminium plates. The detector array was displaced behind a 5 mm thick aluminum plate acting as radiation-shielding, only with a squared opening of 40 mm times 40 mm centred around the aligned laser axis.

#### 1. RCF data Analysis

RCF self-develop under the influence of ionizing radiation and show a change of color (darkening). A key feature is that the changes in the absorption spectrum of a film are bijective with respect to the received dose  $D$ . The films contain sub- $\mu\text{m}$  sized chromophore components that allow a very good spatial localization of the impact of projectiles after radio-synthesis. This means that a space-resolved measurement of the scanning wavelength-dependent optical density  $\iota(\lambda, \vec{x})$  can be transformed into a localized dose measurement  $D(\vec{x})$ . The received total dose is proportional to the so called linear energy transfer (LET) from single projectile-stack interactions. For ion beams, it is possible to retrieve both spectrum and phase space of an ion beam of a known species as the LET in solid state matter is well quantified<sup>67</sup>.

The particularity of ion stopping with respect to electron- and photon-stopping is a maximum of the stopping power for low ion energies with small scattering cross-sections: the stopping power maximum is always located at the end of the penetration range. It is called Bragg-peak<sup>68</sup> and accurately describes the LET of ions in a stack. The film response to ions can be easily distinguished from high-energy background electrons, that may even traverse the stack, as their imprints faint only slowly with increasing depth. Thus the cut-off energy of the ion spectrum  $E^{\text{max}}$  can be estimated from the energy  $E^{\text{out}}$  for which the stopping range corresponds to the depth of the last colored film in the stack. From this energy on, it is possible to de-convolute the particle number density spectrum with respect to projectiles of different energies going from the last imprinted layer to the first imprinted layer in the stack, from high to low energies in the spectrum<sup>51</sup>.

Our data is converted to dose maps with calibration shown in Fig. 25 obtained at a calibrated medical accelerator unit. Fits employ the universal dose response



model<sup>69</sup>

$$\iota_{\text{ch}} = A_{\text{ch}}^{\text{fit}} \cdot \left( 1 - \left( 1 + \frac{D}{k_{\text{ch}}^{\text{fit}}} \right)^\theta \right) + \iota_{0,\text{ch}}^{\text{fit}} \quad (2)$$

The sensitometric curve for the optical density of each color channel  $\iota_{\text{ch}}$  is a function of dose  $D$ . The fit parameters  $A_{\text{ch}}^{\text{fit}}$  and  $k_{\text{ch}}^{\text{fit}}$  depend on channel and scanner system, the off-set  $\iota_{0,\text{ch}}^{\text{fit}}$  depends on the life-cycle of the non-irradiated film and  $\theta = 0.436 \pm 0.005$ <sup>69</sup> represents a universal constant that depends on the sensitive material.

## 2. CR-39 data analysis

CR-39 are made of polyallyl diglycol carbonate polymers with diethylene glycol bis(allyl carbonate) monomer  $\text{C}_{12}\text{H}_{18}\text{O}_7$ . During exposure to ionizing radiation, projectiles collide with the polymer chains and some of them break<sup>70–73</sup>. As a result, the projectile path is permanently imprinted in the plastic with disrupted chains, forming a latent track, and partially damaged chains, forming radicals. Projectiles with a low LET from  $10 \text{ keV } \mu\text{m}^{-1}$  to  $15 \text{ keV } \mu\text{m}^{-1}$  do not lead to the formation of tracks<sup>54</sup>. Thus, single electrons do not produce CR-39 track formation, only electrons in high doses of several kGy trigger radical formation<sup>74</sup>.

Etching the CR-39 with an alkali solution yields ablation of surface material due to reactions of the polymer with the hydroxide ions<sup>70</sup>. The material ablation rate is constant for a pure homogeneous plastic. For exposed regions along tracks with already broken links, the ablation rate is higher and a crater develops, often referred to as etch pit.

Main observables of etch pits at the detector surface are depth, diameter and their evolution with etching time. Observables are bijective with a particular pair of ablation rates and allow to retrieve them along the full projectile track. Such mapping can be compared to calibration data in order to find likely ion species and impact energy ranges. Additionally, the direction of projectiles can be retrieved from the inclination of the crater axis to the detector surface and the ellipticity of the crater.

TasTrak CR-39 Plastic Sheets<sup>75</sup> used for this work are reported to show a good inter-comparability of calibrations<sup>76</sup> to CR-39 of Page Mouldings (Pershore) Limited. This is of further importance as we rely on third-party calibration data<sup>77,78</sup> acquired with CR-39 of Page Mouldings (Pershore) Limited.

We employ NaOH solution of 6.25 N in distilled water for etching the CR-39 from all sides in a bath at constant temperature of  $70^\circ\text{C}$ . For specific etching times in a range from 2 min to 15 h, we take a series of  $447.63 \mu\text{m} \times 335.4 \mu\text{m}$  images acquired in 12 bit with a fully motorized CarlZeiss microscope with approximately  $2 \mu\text{m}$  resolution.

We base a first analysis on the pit diameter evolution with etching time. We select one particular approximately  $20.0 \mu\text{m}$  large etch pit in vicinity of the presumed

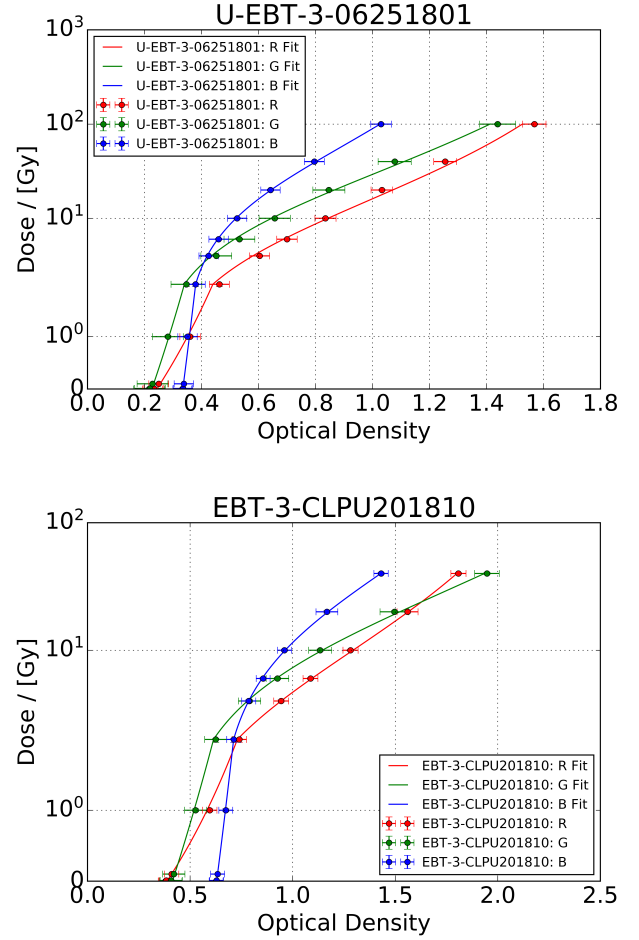


Figure 25. Channel-wise fit of the universal dose response model to calibration data for U-EBT-3 batch number 06251801 (top) and EBT-3 batch number 10251701 (bottom). The dose deposition for calibration data is performed at a medical accelerator unit for clinical oncology based on electron- and photon irradiation at Institut Bergonié, Bordeaux. The dose precision better than 1%. The dose is delivered in bunches of 1 cGy with a dose rate of  $10 \text{ Gy min}^{-1}$  with a macro-bunch length maximum of 50 Gy. Macro-bunches are intersected by a mandatory operator request that takes approximately 10s for performance in average. Scans are acquired with the EPSON EXPRESSION11000XL flat-bed scanner that comprises a cold fluorescent Xenon light source for illumination.

laser axis at 15 h and follow it back in time. Figure 26 shows strioscopic microscope images with the growing pit. Also imaged are several small craters that do not show large growth rates.

The diameter evolution of the large pit corresponds well to the expected evolution for alpha particles of  $5.4(42) \text{ MeV}$  within the margin of the measurement uncertainty, especially due to a diameter underneath the detection limit for 2 h of etching. In the same figure, small etch pits of  $10(5) \mu\text{m}$  are visible that are present even

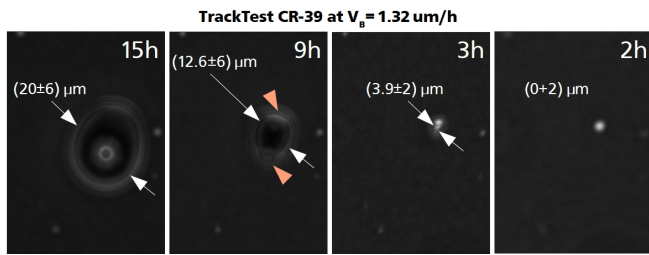


Figure 26. Diameter evolution of an individual etch pit on a TasTrak CR-39 with strioscopic snapshots at 2 h, 3 h, 9 h and 15 h of etching with 6.25 N etchant at 70 °C. The diameter evolves considerably and is not detected for 2 h of etching as it may be underneath the resolution of the microscope system.

for the earliest time, which can not be related to alpha particles. If they belonged to low energy alpha particles, they were expected to grow with about the same growth rate as the finally large etch pit. If they belonged to high energy alpha particles, they should not be visible. Their size does not match any alpha energy nor any energy of Nitrogen projectiles. They could be related to detector material impurities.

In order to confirm the appearance of alpha particles, we choose another typical area far from the laser axis to investigate etch pits with diameters at the detection threshold, see figure 27. The respective dashed circles indicate all etch pits in the field of view, other circular features are microscope artifacts. The circles are located at the same position for both images taken after 2 h and 9 h of etching.

We see that etch pits grow inclined with the surface, their centre shifts with an inclination that is pointing to the laser axis for most pits. Group (a) with already large pits with 5.8(9)  $\mu\text{m}$  diameters for 2 h and slow growth to 6.8(19)  $\mu\text{m}$  for 9 h follows an evolution that suits neither nitrogen nor alpha projectiles. We see craters (b) of 9(6)  $\mu\text{m}$  that are visible for short but not for long etching, which are most likely shallow surface artefacts. Inversely, the most populated group of pits (c) is underneath the detection limit for short etching and reveals pits with diameters from 6(2)  $\mu\text{m}$  to 13(3)  $\mu\text{m}$  for 9 h of etching. Such pits suit either alpha particles with energies from 4 MeV to 40 MeV or nitrogen within an energy range of 15 MeV to 50 MeV. Grouped with (d) are pits that are at the detection limit for 2 h with diameters of 2(2)  $\mu\text{m}$  to 5(2)  $\mu\text{m}$ . The pits grow to 5.8(10)  $\mu\text{m}$  to 7.4(20)  $\mu\text{m}$  after 9 h. Where diameters are well above the microscope resolution, the craters must be very shallow to show a fainting image. Such pits suit nitrogen within an energy range of 1.2 MeV to 2 MeV. Furthermore we see tracks with coherent but different inclination (e), not coming from the presumed laser axis.

It is noteworthy that alpha energies in the MeV range are typical for alpha particles from the decay of natural Radon gas and its chain of decay.  $^{222}\text{Rn}$  has a half life time of 3.824 d and splits into alpha particles of 5.49 MeV

and  $^{218}\text{Po}$ . The pits grouped in (e) may be indeed issued by a chain of radon decay within cm in the vicinity of the CR-39.

A second analysis strategy focuses on a Z-scan of one typical area containing all diameters of craters. We vary the focusing position of the imaging system in  $\mu\text{m}$  steps and follow crater walls from tip to surface to determine the length of the etched tracks. The diameter of pits is determined at the respective etched surface. Results compared to interpolations of calibration data are depicted in figure 28. Data points are underlain with a relative point number density color map in gray-scale and the simulated spectrally resolving species specific  $L(D)$  lobes.

Most etch pits are shallow and of small diameter. Smallest diameters of 3.5(15)  $\mu\text{m}$  belong to craters with a large variation of depth with 4.5(30)  $\mu\text{m}$ . Deeper tracks in a range from 6.0(2)  $\mu\text{m}$  to 12.0(2)  $\mu\text{m}$  form a linear slope with their respective diameters from 4.0(2)  $\mu\text{m}$  to 10.0(2)  $\mu\text{m}$ . Two singular data points with 9.0(2)  $\mu\text{m}$  and 11.0(2)  $\mu\text{m}$  track length do not follow this trend, both of 12.0(2)  $\mu\text{m}$  diameter. Overall, the number density of craters decreases with increasing diameter. In the sample sequence, there is only one crater with a large diameter, here of 23.0(2)  $\mu\text{m}$  and 16.0(2)  $\mu\text{m}$  depth. From the few data points, it is difficult to conclude on a continuous relation between different types of craters.

Larger etch pits show characteristics similar to alpha particles of 4.5(3) MeV and smaller etch pits are in the vicinity of nitrogen projectiles of 56(2) MeV to 200(50) MeV. The data distribution for etch pits with diameters smaller than 10  $\mu\text{m}$  makes it difficult to distinguish with alpha particles of 6.7(3) MeV to 40(14) MeV or nitrogen ions of 56(2) MeV to 100(60) MeV.

## REFERENCES

- <sup>1</sup>Donna Strickland and Gerard Mourou. Compression of amplified chirped optical pulses. *Opt. Commun.*, 56(3):219–221, 1985.
- <sup>2</sup>Hiroyuki Daido, Mamiko Nishiuchi, and Alexander S Pirozhkov. Review of laser-driven ion sources and their applications. *Rep. Prog. Phys.*, 75(5):056401, April 2012.
- <sup>3</sup>Andrea Macchi, Marco Borghesi, and Matteo Passoni. Ion acceleration by superintense laser-plasma interaction. *Rev. Mod. Phys.*, 85:751–793, May 2013.
- <sup>4</sup>M. Borghesi, A. J. Mackinnon, D. H. Campbell, D. G. Hicks, S. Kar, P. K. Patel, D. Price, L. Romagnani, A. Schiavi, and O. Willi. Multi-mev proton source investigations in ultraintense laser-foil interactions. *Phys. Rev. Lett.*, 92:055003, February 2004.
- <sup>5</sup>J J Santos, M Bailly-Grandvaux, L Giuffrida, P Forestier-Colleoni, S Fujioka, Z Zhang, P Korneev, R Bouillaud, S Dorrard, D Batani, M Chevrot, J E Cross, R Crowston, J-L Dubois, J Gazave, G Gregori, E d’Humières, S Hulin, K Ishihara, S Kojima, E Loyer, J-R Marquès, A Morace, P Nicolai, O Peyrusse, A Poyé, D Raffestin, J Ribolzi, M Roth, G Schaumann, F Serres, V T Tikhonchuk, P Vacar, and N Woolsey. Laser-driven platform for generation and characterization of strong quasi-static magnetic fields. *New J. Phys.*, 17(8):083051, aug 2015.
- <sup>6</sup>M. Ehret et al. Picosecond-laser driven ultra-fast em fields prop-

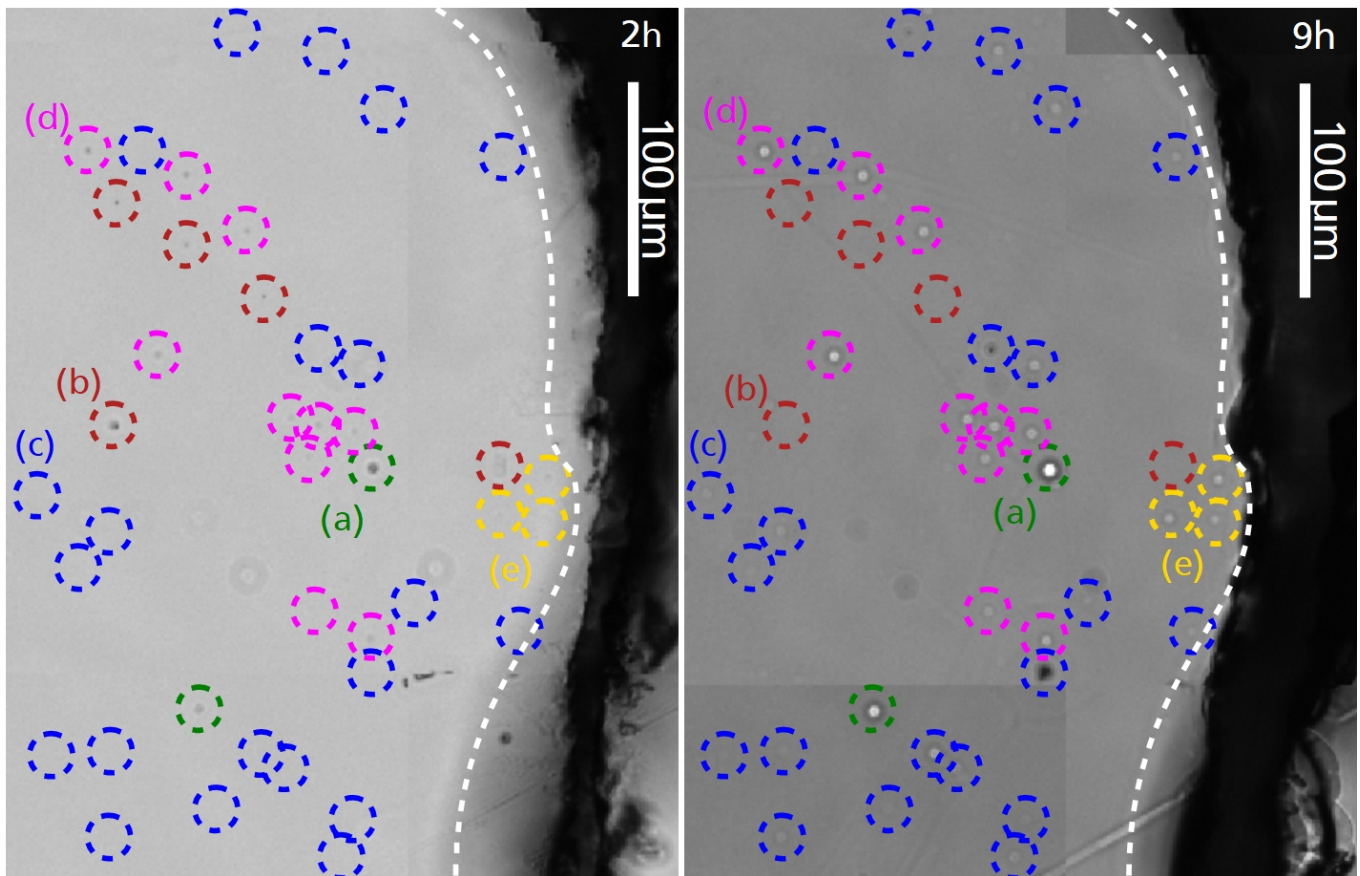


Figure 27. Diameter evolution for similar groups of etch pits on a TasTrak CR-39 with snapshots at 2 h, and 9 h of etching with 6.25 N etchant at 70 °C. Highlighted are groups (a,b,d,e) with circles concentric to the etch pit position for the short etching time and (c) with circles concentric to the pit position for long etching time. The dashed line delimits a scratched area, we do not see the edge of the plastic sheet.

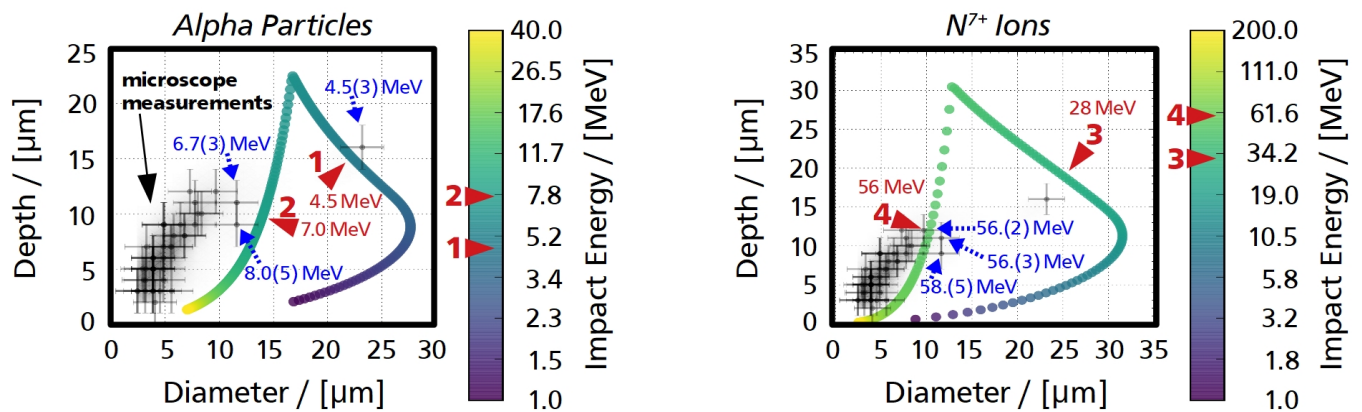


Figure 28. Z-scan of etched pits on a TasTrak CR-39 after 15 h of etching with 6.25 N NaOH etchant at 70 °C. The bulk etching rate was quantified to  $1.32 \mu\text{m h}^{-1}$ . Experimental data points are underlaid with a relative point number density color map in grayscale. The simulated spectrally resolving species specific  $L(D)$  lobes are for alpha particles on the left hand side and for fully ionized Nitrogen ions on the right hand side. Specific impact energies are highlighted with red marker arrows (1–4). Experimental data points that overlap with the lobes in the range of their uncertainty are denoted with the closest corresponding energy on the lobe. Simulated with the CR-39 plug-in of PySTarT.

- agating along coil targets for proton beam micro-lensing. *GSI Scientific Report 2016*, GSI-2017-1:227, 2017.
- <sup>7</sup>P. K. Patel, A. J. Mackinnon, M. H. Key, T. E. Cowan, M. E. Foord, M. Allen, D. F. Price, H. Ruhl, P. T. Springer, and R. Stephens. Isochoric heating of solid-density matter with an ultrafast proton beam. *Phys. Rev. Lett.*, 91:125004, September 2003.
  - <sup>8</sup>M. Roth, T. E. Cowan, M. H. Key, S. P. Hatchett, C. Brown, W. Fountain, J. Johnson, D. M. Pennington, R. A. Snavely, S. C. Wilks, K. Yasuike, H. Ruhl, F. Pegoraro, S. V. Bulanov, E. M. Campbell, M. D. Perry, and H. Powell. Fast ignition by intense laser-accelerated proton beams. *Phys. Rev. Lett.*, 86:436–439, January 2001.
  - <sup>9</sup>K. W. D. Ledingham, P. McKenna, and R. P. Singhal. Applications for nuclear phenomena generated by ultra-intense lasers. *Science*, 300(5622):1107–1111, 2003.
  - <sup>10</sup>I. Spencer, K.W.D. Ledingham, R.P. Singhal, T. McCanny, P. McKenna, E.L. Clark, K. Krushelnick, M. Zepf, F.N. Beg, M. Tatarakis, A.E. Dangor, P.A. Norreys, R.J. Clarke, R.M. Allott, and I.N. Ross. Laser generation of proton beams for the production of short-lived positron emitting radioisotopes. *Nucl. Instrum. Methods Phys. Res. B*, 183(3):449–458, 2001.
  - <sup>11</sup>K. W. D. Ledingham et al. Towards laser driven hadron cancer radiotherapy: A review of progress. *Appl. Sci.*, 4:402–443, 2014.
  - <sup>12</sup>F. Wagner, O Deppert, C Brabetz, P Fiala, A Kleinschmidt, P Poth, VA Schanz, A Tebartz, B Zielbauer, M Roth, et al. Maximum proton energy above 85 mev from the relativistic interaction of laser pulses with micrometer thick ch 2 targets. *Phys. Rev. Lett.*, 116(20):205002, 2016.
  - <sup>13</sup>A Higginson, R.J Gray, M King, R.J Dance, SDR Williamson, NMH Butler, R Wilson, R Capdessus, C Armstrong, JS Green, et al. Near-100 mev protons via a laser-driven transparency-enhanced hybrid acceleration scheme. *Nat. Commun.*, 9(1):1–9, 2018.
  - <sup>14</sup>E. Esarey, C. B. Schroeder, and W. P. Leemans. Physics of laser-driven plasma-based electron accelerators. *Rev. Mod. Phys.*, 81(3):1229–1285, July 2009.
  - <sup>15</sup>K. Krushelnick, E. L. Clark, Z. Najmudin, M. Salvati, M. I. K. Santala, M. Tatarakis, A. E. Dangor, V. Malka, D. Neely, R. Allott, and C. Danson. Multi-MeV Ion Production from High-Intensity Laser Interactions with Underdense Plasmas. *Phys. Rev. Lett.*, 83(4):737–740, July 1999.
  - <sup>16</sup>L. Willingale, S. P. D. Mangles, P. M. Nilson, R. J. Clarke, A. E. Dangor, M. C. Kaluza, S. Karsch, K. L. Lancaster, W. B. Mori, Z. Najmudin, J. Schreiber, A. G. R. Thomas, M. S. Wei, and K. Krushelnick. Collimated multi-mev ion beams from high-intensity laser interactions with underdense plasma. *Phys. Rev. Lett.*, 96:245002, June 2006.
  - <sup>17</sup>A Lifschitz, F Sylla, S Kahaly, A Flacco, M Veltcheva, G Sanchez-Arriaga, E Lefebvre, and V Malka. Ion acceleration in underdense plasmas by ultra-short laser pulses. *New J. Phys.*, 16(3):033031, March 2014.
  - <sup>18</sup>L. Willingale, S. R. Nagel, A. G. R. Thomas, C. Bellei, R. J. Clarke, A. E. Dangor, R. Heathcote, M. C. Kaluza, C. Kamperidis, S. Kneip, K. Krushelnick, N. Lopes, S. P. D. Mangles, W. Nazarov, P. M. Nilson, and Z. Najmudin. Characterization of high-intensity laser propagation in the relativistic transparent regime through measurements of energetic proton beams. *Phys. Rev. Lett.*, 102:125002, March 2009.
  - <sup>19</sup>Fiúza, Frederico and Stockem, Anne and Boella, Elisabetta and Fonseca, RA and Silva, LO and Haberberger, D and Tochitsky, Sergei and Gong, Chao and Mori, Warren B and Joshi, Chandrasekar. Laser-driven shock acceleration of monoenergetic ion beams. *Phys. Rev. Lett.*, 109(21):215001, 2012.
  - <sup>20</sup>A Debayle, F Mollica, B Vauzour, Y Wan, A Flacco, V Malka, X Davoine, and L Gremillet. Electron heating by intense short-pulse lasers propagating through near-critical plasmas. *New J. Phys.*, 19(12):123013, December 2017.
  - <sup>21</sup>O N Rosmej, N E Andreev, S Zaehter, N Zahn, P Christ, B Borm, T Radon, A Sokolov, L P Pugachev, D Khaghani, F Horst, N G Borisenko, G Sklizkov, and V G Pimenov. Interaction of relativistically intense laser pulses with long-scale near critical plasmas for optimization of laser based sources of MeV electrons and gamma-rays. *New J. Phys.*, 21(4):043044, April 2019.
  - <sup>22</sup>Andrea Pazzaglia, Luca Fedeli, Arianna Formenti, Alessandro Maffini, and Matteo Passoni. A theoretical model of laser-driven ion acceleration from near-critical double-layer targets. *Commun. Phys.*, 3(1):133, August 2020.
  - <sup>23</sup>S. S. Moiseev and R. Z. Sagdeev. Collisionless shock waves in a plasma in a weak magnetic field. *J. Nucl. Energy*, 5(1):43–47, January 1963.
  - <sup>24</sup>D. W. Forslund and C. R. Shonk. Formation and Structure of Electrostatic Collisionless Shocks. *Phys. Rev. Lett.*, 25(25):1699–1702, December 1970.
  - <sup>25</sup>G Sorasio, Michael Marti, Ricardo Fonseca, and Luis O Silva. Very high mach-number electrostatic shocks in collisionless plasmas. *Phys. Rev. Lett.*, 96(4):045005, 2006.
  - <sup>26</sup>R. A. Cairns, R. Bingham, P. Norreys, and R. Trines. Laminar shocks in high power laser plasma interactions. *Phys. Plasmas*, 21(2):022112, February 2014.
  - <sup>27</sup>Luis O. Silva, Michael Marti, Jonathan R. Davies, Ricardo A. Fonseca, Chuang Ren, Frank S. Tsung, and Warren B. Mori. Proton shock acceleration in laser-plasma interactions. *Phys. Rev. Lett.*, 92:015002, January 2004.
  - <sup>28</sup>F. Fiuza, A. Stockem, E. Boella, R. A. Fonseca, L. O. Silva, D. Haberberger, S. Tochitsky, W. B. Mori, and C. Joshi. Ion acceleration from laser-driven electrostatic shocks. *Phys. Plasmas*, 20(5):056304, May 2013.
  - <sup>29</sup>Young-Kuk Kim, Teyoun Kang, Moon Youn Jung, and Min Sup Hur. Effects of laser polarizations on shock generation and shock ion acceleration in overdense plasmas. *Phys. Rev. E*, 94(3):033211, 2016.
  - <sup>30</sup>M. Liu, S. M. Weng, Y. T. Li, D. W. Yuan, M. Chen, P. Mulser, Z. M. Sheng, M. Murakami, L. L. Yu, X. L. Zheng, and J. Zhang. Collisionless electrostatic shock formation and ion acceleration in intense laser interactions with near critical density plasmas. *Phys. Plasmas*, 23(11):113103, 2016.
  - <sup>31</sup>A. Pak, S. Kerr, N. Lemos, A. Link, P. Patel, F. Albert, L. Divol, B. B. Pollock, D. Haberberger, D. Froula, M. Gauthier, S. H. Glenzer, A. Longman, L. Manzoor, R. Fedosejevs, S. Tochitsky, C. Joshi, and F. Fiuza. Collisionless shock acceleration of narrow energy spread ion beams from mixed species plasmas using  $\mu\text{m}$  lasers. *Phys. Rev. Accel. Beams*, 21:103401, October 2018.
  - <sup>32</sup>P. Antici, E. Boella, S. N. Chen, D. S. Andrews, M. Barberio, J. Böker, F. Cardelli, J. L. Feuges, M. Glesser, P. Nicolai, L. Romagnani, M. Scisciò, M. Starodubtsev, O. Willi, J. C. Kieffer, V. Tikhonchuk, H. Pépin, L. O. Silva, E. d’Humières, and J. Fuchs. Acceleration of collimated 45 MeV protons by collisionless shocks driven in low-density, large-scale gradient plasmas by a  $10^{20} \text{ W/cm}^2$ ,  $1 \mu\text{m}$  laser. *Sci. Rep.*, 7:16463, November 2017.
  - <sup>33</sup>S. N. Chen, M. Vranic, T. Gangolf, E. Boella, P. Antici, M. Bailly-Grandvaux, P. Loiseau, H. Pépin, G. Revet, J. J. Santos, A. M. Schroer, Mikhail Starodubtsev, O. Willi, L. O. Silva, E. d’Humières, and J. Fuchs. Collimated protons accelerated from an overdense gas jet irradiated by a  $1 \mu\text{m}$  wavelength high-intensity short-pulse laser. *Sci. Rep.*, 7:13505, October 2017.
  - <sup>34</sup>P. Puyuelo-Valdes, J. L. Henares, F. Hannachi, T. Ceccotti, J. Domange, M. Ehret, E. d’Humières, L. Lancia, J.-R. Marquès, X. Ribeyre, J. J. Santos, V. Tikhonchuk, and M. Tarisien. Proton acceleration by collisionless shocks using a supersonic h2 gas-jet target and high-power infrared laser pulses. *Phys. Plasmas*, 26(12):123109, 2019.
  - <sup>35</sup>Stepan S. Bulanov, Valery Yu. Bychenkov, Vladimir Chvykov, Galina Kalinchenko, Dale William Litzenberg, Takeshi Matsumoto, Alexander G. R. Thomas, Louise Willingale, Victor Yanovsky, Karl Krushelnick, and Anatoly Maksimchuk. Generation of gev protons from 1 pw laser interaction with near critical density targets. *Phys. Plasmas*, 17(4):043105, 2010.
  - <sup>36</sup>Tatsufumi Nakamura, Sergei V. Bulanov, Timur Zh. Esirkepov, and Masaki Kando. High-energy ions from near-critical den-

- sity plasmas via magnetic vortex acceleration. *Phys. Rev. Lett.*, 105:135002, September 2010.
- <sup>37</sup>F. Sylla, A. Flacco, S. Kahaly, M. Veltcheva, A. Lifschitz, G. Sanchez-Arriaga, E. Lefebvre, and V. Malka. Anticorrelation between ion acceleration and nonlinear coherent structures from laser-underdense plasma interaction. *Phys. Rev. Lett.*, 108:115003, March 2012.
- <sup>38</sup>M. H. Helle, D. F. Gordon, D. Kaganovich, Y. Chen, J. P. Palastro, and A. Ting. Laser-accelerated ions from a shock-compressed gas foil. *Phys. Rev. Lett.*, 117:165001, October 2016.
- <sup>39</sup>J. Park, S. S. Bulanov, J. Bin, Q. Ji, S. Steinke, J.-L. Vay, C. G. R. Geddes, C. B. Schroeder, W. P. Leemans, T. Schenkel, and E. Esarey. Ion acceleration in laser generated megatesla magnetic vortex. *Phys. Plasmas*, 26(10):103108, 2019.
- <sup>40</sup>E d’Humières and P Antici and M Glesser and J Boeker and F Cardelli and S Chen and J L Feugeas and F Filippi and M Gauthier and A Levy and P Nicolai and H Pépin and L Romagnani and M Scisciò and V T Tikhonchuk and O Willi and J C Kieffer and J Fuchs. Investigation of laser ion acceleration in low-density targets using exploded foils. *Plasma Phys. Control. Fusion*, 55(12):124025, November 2013.
- <sup>41</sup>Gauthier, M. and Lévy, A. and d’Humières, E. and Glesser, M. and Albertazzi, B. and Beaucourt, C. and Breil, J. and Chen, S. N. and Dervieux, V. and Feugeas, J. L. and Nicolai, P. and Tikhonchuk, V. and Pépin, H. and Antici, P. and Fuchs, J. Investigation of longitudinal proton acceleration in exploded targets irradiated by intense short-pulse laser. *Phys. Plasmas*, 21(1):013102, 2014.
- <sup>42</sup>I Principe and A Sgattoni and D Dellasega and L Fedeli and L Cialfi and Il Woo Choi and I Jong Kim and K A Janulewicz and K F Kakolee and Hwang Woon Lee and Jae Hee Sung and Seong Ku Lee and Chang Hee Nam and M Passoni. Development of foam-based layered targets for laser-driven ion beam production. *Plasma Phys. Controlled Fusion*, 58(3):034019, February 2016.
- <sup>43</sup>J. H. Bin, W. J. Ma, H. Y. Wang, M. J. V. Streeter, C. Kreuzer, D. Kiefer, M. Yeung, S. Cousins, P. S. Foster, B. Dromey, X. Q. Yan, R. Ramis, J. Meyer-ter-Vehn, M. Zepf, and J. Schreiber. Ion Acceleration Using Relativistic Pulse Shaping in Near-Critical-Density Plasmas. *Phys. Rev. Lett.*, 115(6):064801, August 2015.
- <sup>44</sup>J. H. Bin, M. Yeung, Z. Gong, H. Y. Wang, C. Kreuzer, M. L. Zhou, M. J. V. Streeter, P. S. Foster, S. Cousins, B. Dromey, J. Meyer-ter-Vehn, M. Zepf, and J. Schreiber. Enhanced Laser-Driven Ion Acceleration by Superponderomotive Electrons Generated from Near-Critical-Density Plasma. *Phys. Rev. Lett.*, 120(7):074801, February 2018.
- <sup>45</sup>A. J. Goers, G. A. Hine, L. Feder, B. Miao, F. Salehi, J. K. Wahlstrand, and H. M. Milchberg. Multi-mev electron acceleration by subterawatt laser pulses. *Phys. Rev. Lett.*, 115:194802, November 2015.
- <sup>46</sup>J. L. Henaes, P. Puyuelo-Valdes, F. Hannachi, T. Ceccotti, M. Ehret, F. Gobet, L. Lancia, J.-R. Marquès, J. J. Santos, M. Versteegen, and M. Tarisien. Development of gas jet targets for laser-plasma experiments at near-critical density. *Rev. Sci. Instrum.*, 90(6):063302, 2019.
- <sup>47</sup>F Sylla, M Veltcheva, S Kahaly, Alessandro Flacco, and Victor Malka. Development and characterization of very dense submillimetric gas jets for laser-plasma interaction. *Rev. Sci. Instrum.*, 83(3):033507, 2012.
- <sup>48</sup>L. Volpe, R. Fedosejevs, G. Gatti, J. A. Pérez-Hernández, C. Méndez, J. Apiñaniz, X. Vaisseau, C. Salgado, M. Huault, S. Malko, and et al. Generation of high energy laser-driven electron and proton sources with the 200 tw system vega 2 at the centro de laseres pulsados. *High Power Laser Sci. Eng.*, 7:e25, 2019.
- <sup>49</sup>J. Primot et al. L’analyse de surface d’onde par interférométrie à décalage multilatéral. *Photoniques (Orsay)*, 2005.
- <sup>50</sup>I. H. Hutchinson. *Principles of Plasma Diagnostics*. Cambridge University Press, 2 edition, 2002.
- <sup>51</sup>F. Nürnberg et al. Radiochromic film imaging spectroscopy of laser-accelerated proton beams. *Rev. Sci. Instrum.*, 80(033301), March 2009.
- <sup>52</sup>D. A. Young. Etching of radiation damage in lithium fluoride. *Nature*, 182(4632):375–377, August 1958.
- <sup>53</sup>S. A. Durrani and R. K. Bull. *Solid State Nuclear Track Detection*. Pergamon, 1987.
- <sup>54</sup>M. Hajek et al. Convolution of tld and ssntd measurements during the brados-1 experiment onboard iss (2001). *Radiat. Meas.*, 43(7):1231–1236, 2008.
- <sup>55</sup>L. Porter. *GAFCHROMIC DOSIMETRY MEDIA, TYPE EBT-3*. Ashland, February 2016.
- <sup>56</sup>Films were made available to us by the Advanced Materials Group of Ashland Specialty Ingredients G.P., 1005 US Hwy No 202/206, Bridgewater, NJ 08807, USA.
- <sup>57</sup>K. Mehta and I. Janovský. Measurements of electron depth-dose distributions in thick plastics and effects of accumulated charge. *Radiat. Phys. Chem.*, 47(3):487 – 490, 1996. Tihany Symposium on Radiation Chemistry.
- <sup>58</sup>E Lefebvre, N Cochet, S Fritzler, Victor Malka, M-M Aléonard, J-F Chemin, S Darbon, L Disdier, Jérôme Faure, A Fedotoff, et al. Electron and photon production from relativistic laser-plasma interactions. *Nucl. Fusion*, 43(7):629, 2003.
- <sup>59</sup>L. Jonušauskas et al. Mesoscale laser 3d printing. *Opt. Express*, 27(11):15205–15221, May 2019.
- <sup>60</sup>R.D. Saini and P.K. Bhattacharyya. Radiolytic oxidation of u(iv) sulphate in aqueous solution by alpha particles from cyclotron. *Int. J. Radiat. Appl. Instrum. C.*, 29(5):375 – 379, 1987.
- <sup>61</sup>G. Baldacchino. Pulse radiolysis in water with heavy-ion beams. a short review. *Radiat. Phys. Chem.*, 77(10):1218 – 1223, 2008. The International Symposium on Charged Particle and Photon Interaction with Matter - ASR 2007.
- <sup>62</sup>P. Boller, A. Zylstra, P. Neumaye, et al. First on-line detection of radioactive fission isotopes produced by laser-accelerated protons. *Sci. Rep.*, (10):17183, 2020.
- <sup>63</sup>J. Chatal et al. Alphatherapy, the new impetus to targeted radionuclide therapy? *Eur. J. Nucl. Med. Mol. Imaging*, (45):1362–1363, 2018.
- <sup>64</sup>IAEA. Medical physics staffing needs in diagnostic imaging and radionuclide therapy: an activity based approach. Technical report, 2018.
- <sup>65</sup>M. Makvandi et al. Alpha-emitters and targeted alpha therapy in oncology: from basic science to clinical investigations. *Target. Oncol.*, (13):189–203, 2018.
- <sup>66</sup>DM Corallo, DM Creek, and GM Murray. The x-ray calibration of silicon pin diodes between 1.5 and 17.4 kev. *J. Phys. E: Sci. Instrum.*, 13(6):623, 1980.
- <sup>67</sup>J. F. Ziegler. The stopping of energetic light ions in elemental matter. *Rev. Appl. Phys.*, 85:1249–1272, 1999.
- <sup>68</sup>P. Sigmund. *Particle Penetration and Radiation Effects*. Number 151 in Solid State Sciences. Berlin Heidelberg : Springer-Verlag, 2006.
- <sup>69</sup>J. A. Martín-Viera Cueto et al. A universal dose–response curve for radiochromic films. *Med. Phys.*, 42(1):221–231, 2015.
- <sup>70</sup>J. Stejny and T. Portwood. A study of the molecular structure in cr-39. *Int. J. Radiat. Appl. Instrum. Part D*, 12(1):121–123, 1986. Special Volume Solid State Nuclear Track Detectors.
- <sup>71</sup>W. Maurer. Neutron and gamma irradiation effects onorganic insulating materials for fusionmagnets. TECDOC 417, KIT, International Atomic Energy Agency, Vienna, 1987.
- <sup>72</sup>N. X. Thang and T. T. Doan. Structure effect in response function of cr-39 detector. *Radiat. Meas.*, 25(1):185–187, 1995. Nuclear Tracks in Solids.
- <sup>73</sup>C. S. Chong et al. Uv-vis and ftir spectral studies of cr-39 plastics irradiated with x-rays. *Radiat. Meas.*, 28(1):119–122, 1997. International Conference on Nuclear Tracks in Solids.
- <sup>74</sup>J. Charvát and F. Spurný. Etching characteristics of cellulose nitrate and cr-39 after high dose electron irradiation. *Int. J. Radiat. Appl. Instrum. Part D*, 14(4):451–455, 1988.
- <sup>75</sup>A. Worley. Tastrak material safety data sheet msds-070314-1 (revision 12). Technical report, TASL, Napier House Meadow Grove Shirehampton Bristol BS11 9PJ, 2014.
- <sup>76</sup>Y. Zhang et al. Energy calibration of a cr-39 nuclear-track de-

- tector irradiated by charged particles. *Nucl. Sci. Tech.*, (30):87, 2019.
- <sup>77</sup>A. A. Azooz, S. H. Al-Nia'emi, and M. A. Al-Jubbori. Empirical parameterization of cr-39 longitudinal track depth. *Radiat. Meas.*, 47(1):67–72, 2012.
- <sup>78</sup>A. A. Azooz, D. Hermsdorf, and M. A. Al-Jubbori. New approach of modeling charged particles track development in cr-39 detectors. *Radiat. Meas.*, 58:94–100, 2013.